1 **Development and evaluation of a variably saturated flow model in the global**

2 **E3SM Land Model (ELM) Version 1.0**

4 **Gautam Bisht[1], William J. Riley[1], Glenn E. Hammond[2], and David M. Lorenzetti[3]**

6 [1]Climate & Ecosystem Sciences Division, Lawrence Berkeley National Laboratory,1

7 Cyclotron Road, Berkeley, California 94720, USA

9 [2]Applied Systems Analysis and Research Department, Sandia National Laboratories,

10 Albuquerque, NM 87185-0747, USA

12 [3]Sustainable Energy Systems Group, Lawrence Berkeley National Laboratory,1

13 Cyclotron Road, Berkeley, California 94720, USA

15 Correspondence to: Gautam Bisht (gbisht@lbl.gov)

Abstract

Improving global-scale model representations of near-surface soil moisture and groundwater hydrology is important for accurately simulating terrestrial processes and predicting climate change effects on water resources. Most existing land surface models, including the default E3SM Land Model (ELMv0), which we modify here, routinely employ different formulations for water transport in the vadose and phreatic zones. Clark et al. (2015) identified a variably saturated Richards equation flow model as an important capability for improving simulation of coupled soil moisture and shallow groundwater dynamics. In this work, we developed the Variably Saturated Flow Model (VSFM) in ELMv1 to unify the treatment of soil hydrologic processes in the unsaturated and saturated zones. VSFM was tested on three benchmark problems and results were evaluated against observations and an existing benchmark model (PFLOTRAN). The ELMv1-VSFM's subsurface drainage parameter, f_d, was calibrated to match an observationally-constrained and spatially-explicit global water table depth (WTD) product. Optimal spatially-explicit f_d values were obtained for 79% of global $1.9^0 \times 2.5^0$ gridcells, while the remaining 21% of global gridcells had predicted WTD deeper than the observationally-constrained estimate. Comparison with predictions using the default f_d value demonstrated that calibration significantly improved predictions, primarily by allowing much deeper WTDs. Model evaluation using the International Land Model Benchmarking package (ILAMB) showed that improvements in WTD predictions did not degrade model skill for any other metrics. We evaluated the computational performance of the VSFM model and found that the model is about 30% more expensive than the default ELMv0 with an optimal processor layout. The modular software design of VSFM not only provides flexibility to configure the model for a range of problem setups, but also allows building the model independently of the ELM code, thus enabling straightforward testing of model's physics against other models.

1 Introduction

Groundwater, which accounts for 30% of freshwater reserves globally, is a vital human water resource. It is estimated that groundwater provides 20-30% of global freshwater withdrawals (Petra, 2009; Zektser and Evertt, 2004), and that irrigation accounts for ~70% of these withdrawals (Siebert et al., 2010). Climate change is expected to impact the quality and quantity of groundwater in the future (Alley, 2001). As temporal variability of precipitation and surface water increases in the future due to climate change, reliance on groundwater as a source of fresh water for domestic, agriculture, and industrial use is expected to increase (Taylor et al., 2013).

Local environmental conditions modulate the impact of rainfall changes on groundwater resources. For example, high intensity precipitation in humid areas may lead to a decrease in groundwater recharge (due to higher surface runoff), while arid regions are expected to see gains in groundwater storage (as infiltrating water quickly travels deep into the ground before it can be lost to the atmosphere) (Kundzewicz and Doli, 2009). Although global climate models predict changes in precipitation over the next century (Marvel et al., 2017), few global models that participated in the recent Coupled Model Inter-comparison Project (CMIP5; Taylor et al. (2012)) were able to represent global groundwater dynamics accurately (e.g. Swenson and Lawrence (2014))

Modeling studies have also investigated impacts, at watershed to global scales, on future groundwater resources associated with land-use (LU) and land-cover (LC) change (Dams et al., 2008) and ground water pumping (Ferguson and Maxwell, 2012; Leng et al., 2015). Dams et al. (2008) predicted that LU changes would result in a small mean decrease in subsurface recharge and large spatial and temporal variability in groundwater depth for the Kleine Nete basin in Belgium. Ferguson and Maxwell (2012) concluded that groundwater-fed irrigation impacts on water exchanges with the atmosphere and groundwater resources can be comparable to those from a 2.5 °C increase in air temperature for the Little Washita basin in Oklahoma, USA. By performing global simulations of climate change scenarios using CLM4, Leng et al. (2015) concluded that the water source (i.e., surface or groundwater) used for

73   irrigation depletes the corresponding water source while increasing the storage of

74   the other water source. Recently, Leng et al. (2017) showed that irrigation method

75   (drip, sprinkler, or flood) has impacts on water balances and water use efficiency in

76   global simulations.

77   Groundwater models are critical for developing understanding of

78   groundwater systems and predicting impacts of climate (Green et al., 2011). Kollet

79   and Maxwell (2008) identified critical zones, i.e., regions within the watershed with

80   water table depths between $1-5$ m, where the influence of groundwater dynamics

81   was largest on surface energy budgets. Numerical studies have demonstrated impacts

82   of groundwater dynamics on several key Earth system processes, including soil

83   moisture (Chen and Hu, 2004; Liang et al., 2003; Salvucci and Entekhabi, 1995; Yeh

84   and Eltahir, 2005), runoff generation (Levine and Salvucci, 1999; Maxwell and Miller,

85   2005; Salvucci and Entekhabi, 1995; Shen et al., 2013), surface energy budgets

86   (Alkhaier et al., 2012; Niu et al., 2017; Rihani et al., 2010; Soylu et al., 2011), land-

87   atmosphere interactions (Anyah et al., 2008; Jiang et al., 2009; Leung et al., 2011;

88   Yuan et al., 2008), vegetation dynamics (Banks et al., 2011; Chen et al., 2010), and soil

89   biogeochemistry (Lohse et al., 2009; Pacific et al., 2011).

90   Recognizing the importance of groundwater systems on terrestrial processes,

91   groundwater models of varying complexity have been implemented in land surface

92   models (LSMs) in recent years. Groundwater models in current LSMs can be classified

93   into four categories based on their governing equations. Type-1 models assume a

94   quasi-steady state equilibrium of the soil moisture profile above the water table

95   (Hilberts et al., 2005; Koster et al., 2000; Walko et al., 2000). Type-2 models use a θ-

96   based (where θ is the water volume content) Richards equation in the unsaturated

97   zone coupled with a lumped unconfined aquifer model in the saturated zone.

98   Examples of one-dimensional Type-2 models include Liang et al. (2003), Yeh and

99   Eltahir (2005), Niu et al. (2007), and Zeng and Decker (2009). Examples of quasi

100   three-dimensional Type-2 models are York et al. (2002); Fan et al. (2007); Miguez-

101   Macho et al. (2007); and Shen et al. (2013). Type-3 models include a three-

102   dimensional representation of subsurface flow based on the variably saturated

103   Richards equation (Maxwell and Miller, 2005; Tian et al., 2012). Type-3 models

104   employ a unified treatment of hydrologic processes in the vadose and phreatic zones

105   but lump changes associated with water density and unconfined aquifer porosity into

106   a specific storage term. The fourth class (Type-4) of subsurface flow and reactive

107   transport models (e.g., PFLOTRAN (Hammond and Lichtner, 2010), TOUGH2 (Pruess

108   et al., 1999), and STOMP (White and STOMP, 2000)) combine a water equation of

109   state (EoS) and soil compressibility with the variably saturated Richards equation.

110   Type-4 models have not been routinely coupled with LSMs to address climate change

111   relevant research questions. Clark et al. (2015) summarized that most LSMs use

112   different physics formulations for representing hydrologic processes in saturated and

113   unsaturated zones. Additionally, Clark et al. (2015) identified incorporation of

114   variably saturated hydrologic flow models (i.e., Type-3 and Type-4 models) in LSMs

115   as a key opportunity for future model development that is expected to improve

116   simulation of coupled soil moisture and shallow groundwater dynamics.

117   The Energy, Exascale, Earth System Model (E3SM) is a new Earth System

118   Modeling project sponsored by the U.S. Department of Energy (DOE) (E3SM Project,

119   2018). The E3SM model started from the Community Earth System Model (CESM)

120   version 1_3_beta10 (Oleson, 2013). Specifically, the initial version (v0) of the E3SM

121   Land Model (ELM) was based off the Community Land Model's (CLM's) tag 4_5_71.

122   ELMv0 uses a Type-2 subsurface hydrology model based on Zeng and Decker (2009).

123   In this work, we developed in ELMv1 a Type-4 Variably Saturated Flow model (VSFM)

124   to provide a unified treatment of soil hydrologic processes within the unsaturated

125   and saturated zones. The VSFM formulation is based on the isothermal, single phase,

126   variably-saturated (RICHARDS) flow model within PFLOTRAN (Hammond and

127   Lichtner, 2010). While PFLOTRAN is a massively parallel, three-dimensional

128   subsurface model, the VSFM is a serial, one-dimensional model that is appropriate for

129   climate scale applications.

130   This paper is organized into several sections: (1) brief review of the ELMv0

131   subsurface hydrology model; (2) overview of the VSFM formulation integrated in

132   ELMv1; (3) application of the new model formulation to three benchmark problems;

133   (4) development of a subsurface drainage parameterization necessary to predict

134 global water table depths (WTDs) comparable to recently released observationally-
135 constrained estimates; (5) comparison of ELMv1 global simulations with the default
136 subsurface hydrology model and VSFM against multiple observations using the
137 International Land Model Benchmarking package (ILAMB; Hoffman et al. (2017));
138 and (6) a summary of major findings.

139 2 Methods

140 2.1 Current Model Formulation

141 Water flow in the unsaturated zone is often described by the θ-based Richards
142 equation:

$$\frac{\partial \theta}{\partial t} = -\nabla \cdot \boldsymbol{q} - Q \tag{1}$$

143

144 where θ [m³ of water m⁻³ of soil] is the volumetric soil water content, t [s] is time, $\boldsymbol{q}$
145 [m s⁻¹] is the Darcy water flux, and Q [m³ of water m⁻³ of soil s⁻¹] is a soil moisture
146 sink term. The Darcy flux, $\vec{q}$, is given by

$$\boldsymbol{q} = -K\nabla(\psi + z) \tag{2}$$

147 where K [ms⁻¹] is the hydraulic conductivity, z [m] is height above some datum in the
148 soil column and ψ [m] is the soil matric potential. The hydraulic conductivity and soil
149 matric potential are modeled as non-linear function of volumetric soil moisture
150 following Clapp and Hornberger (1978):

$$K = \Theta_{ice} K_{sat} \left(\frac{\theta}{\theta_{sat}} \right)^{2B+3} \tag{3}$$

$$\psi = \psi_{sat} \left(\frac{\theta}{\theta_{sat}} \right)^{-B} \tag{4}$$

151

152 where K_{sat} [m s⁻¹] is saturated hydraulic conductivity, ψ_{sat} [m] is saturated soil
153 matric potential, B is a linear function of percentage clay and organic content (Oleson,
154 2013), and Θ_{ice} is the ice impedance factor (Swenson et al., 2012). ELMv0 uses the

155 modified form of Richards equation of Zeng and Decker (2009) that computes Darcy
156 flux as

$$\boldsymbol{q} = -K\boldsymbol{\nabla}(\psi + z - C) \tag{5}$$

157 where C is a constant hydraulic potential above the water table, z_∇, given as

$$C = \psi_E + z = \psi_{sat}\left(\frac{\theta_E(z)}{\theta_{sat}}\right)^{-B} + z = \psi_{sat} + z_\nabla \tag{6}$$

158 where ψ_E [m] is the equilibrium soil matric potential, z [m] is height above a
159 reference datum, θ_E [m³ m⁻³] is volumetric soil water content at equilibrium soil
160 matric potential, and z_∇ [m] is height of water table above a reference datum. ELMv0
161 uses a cell-centered finite volume spatial discretization and backward Euler implicit
162 time integration. By default, ELMv0's vertical discretization of a soil column yields 15
163 soil layers of exponentially varying soil thicknesses that reach a depth of 42.1 m Only
164 the first 10 soils layers (or top 3.8 m of each soil column), are hydrologically active,
165 while thermal processes are resolved for all 15 soils layers. The nonlinear Darcy flux
166 is linearized using Taylor series expansion and the resulting tridiagonal system of
167 equations is solved by LU factorization.

168   Flow in the saturated zone is modeled as an unconfined aquifer below the soil
169 column based on the work of Niu et al. (2007). Exchange of water between the soil
170 column and unconfined aquifer depends on the location of the water table. When the
171 water table is below the last hydrologically active soil layer in the column, a recharge
172 flux from the last soil layer replenishes the unconfined aquifer. A zero-flux boundary
173 condition is applied to the last hydrologically active soil layer when the water table is
174 within the soil column. The unconfined aquifer is drained by a flux computed based
175 on the SIMTOP scheme of Niu et al. (2007) with modifications to account for frozen
176 soils (Oleson, 2013).

177 **2.2   New VSFM Model Formulation**

178 In the VSFM formulation integrated in ELMv1, we use the mass conservative form of
179 the variably saturated subsurface flow equation (Farthing et al., 2003; Hammond and
180 Lichtner, 2010; Kees and Miller, 2002):

$$\frac{\partial(\phi s_w \rho)}{\partial t} = -\nabla \cdot (\rho \boldsymbol{q}) - Q \tag{7}$$

181 where ϕ [m³ m⁻³] is the soil porosity, s_w [-] is saturation, ρ [kg m⁻³] is water density,

182 $\boldsymbol{q}$ [m s⁻¹] is the Darcy velocity, and Q [kg m⁻³ s⁻¹] is a water sink. We restrict our model

183 formulation to a one-dimensional system and the flow velocity is defined by Darcy's

184 law:

$$\boldsymbol{q} = -\frac{k k_r}{\mu} \nabla(P + \rho gz) \tag{8}$$

185 where k [m²] is intrinsic permeability, k_r [-] is relative permeability, μ [Pa s] is

186 viscosity of water, P [Pa] is pressure, g [m s⁻²] is the acceleration due to gravity, and

187 z [m] is elevation above some datum in the soil column.

188   In order to close the system, a constitutive relationship is used to express

189 saturation and relative permeability as a function of soil matric pressure. Analytic

190 Water Retention Curves (WRCs) are used to model effective saturation (s_e)

$$s_e = \left(\frac{s_w - s_r}{1 - s_r}\right) \tag{9}$$

191 where s_w is saturation and s_r is residual saturation. We have implemented Brooks

192 and Corey (1964) (equation 10) and van Genuchten (1980) (equation 11) WRCs:

$$s_e = \begin{cases} \left(\frac{-P_c}{P_c^0}\right)^{-\lambda} & if \ P_c < \ P_c^0 \\ 1 & if \ P_c \geq \ 0 \end{cases} \tag{10}$$

$$s_e = \begin{cases} [1 + (\alpha|P_c|)^n]^{-m} & if \ P_c < \ 0 \\ 1 & if \ P_c \geq \ 0 \end{cases} \tag{11}$$

193 where P_c [Pa] is the capillary pressure, P_c^0 [Pa] is the air entry pressure, and α [Pa⁻¹]

194 is inverse of the air entry pressure, λ [-] is the exponent in the Brooks and Corey

195 parameterization, and n [-] and m [-] are van Genuchten parameters. The capillary

196 pressure is computed as $P_c = P - P_{ref}$ where P_{ref} is P_c^0 for Brooks and Corey WRC

197 and typically the atmospheric pressure (=101,325 [Pa]) is used for van Genuchten

198 WRC. In addition, a smooth approximation of equation (10) and (11) was developed

199 to facilitate convergence of the nonlinear solver (Appendix A). Relative soil

200 permeability was modeled using the Mualem (1976) formulation:

$$\kappa_r(s_e) = \begin{cases} s_e{}^{0.5} \left[1 - \left(1 - s_e^{1/m} \right)^m \right] & if \; P < P_{ref} \\ 1 & if \; P \geq P_{ref} \end{cases} \tag{12}$$

201   where $m = 1 - 1/n$. Lastly, we used an EoS for water density, ρ, that is a nonlinear

202   function of liquid pressure, P, and liquid temperature, T, given by Tanaka et al.

203   (2001):

$$\rho(P,T) = \left[1 + (k_0 + k_1 T + k_2 T^2)(P - P_{ref}) \right] a_5 \left[1 - \frac{(T + a_1)^2 (T + a_2)}{a_3 (T + a_4)} \right] \tag{13}$$

204   where

$$k_0 = 50.74 \times 10^{-11} \; [\text{Pa}^{-1}]$$
$$k_1 = -0.326 \times 10^{-11} \; [\text{Pa}^{-1}\text{C}^{-1}]$$
$$k_2 = 0.00416 \times 10^{-11} \; [\text{Pa}^{-1}\text{C}^2]$$
$$a_1 = -3.983035 \; [\text{C}]$$
$$a_2 = 301.797 \; [\text{C}]$$
$$a_3 = 522558.9 \; [\text{C}^{-2}]$$
$$a_4 = 69.34881 \; [\text{C}]$$
$$a_5 = 999.974950 \; [\text{kg m}^{-3}]$$

205   The sink of water due to transpiration from a given plant functional type (PFT)

206   is vertically distributed over the soil column based on area and root fractions of the

207   PFT. The top soil layer has an additional flux associated with balance of infiltration

208   and soil evaporation. The subsurface drainage flux is applied proportionally to all soil

209   layers below the water table. Details on the computation of water sinks are given in

210   Oleson (2013) Unlike the default subsurface hydrology model, the VSFM is applied

211   over the full sol depth (in the default model, 15 soils layers). The VSFM model replaces

212   both the θ-based Richards equation and the unconfined aquifer of the default model

213   and uses a zero-flux lower boundary condition. In the VSFM model, water table depth

214   is diagnosed based on the vertical soil liquid pressure profile. Like the default model,

215   drainage flux is computed based on the modified SIMTOP approach and is vertically

216   distributed over the soil layers below the water table.

2.2.1 Discrete Equations

We use a cell-centered finite volume discretization to decompose the spatial domain, Ω, into N non-overlapping control volumes, Ω_n, such that $\Omega = \cup_{n=1}^{N} \Omega_i$ and Γ_n represents the boundary of the n-th control volume. Applying a finite volume integral to equation (7) and the divergence theorem yields

$$\frac{\partial}{\partial t} \int_{\Omega_n} (\phi s_w \rho) \, dV = - \int_{\Gamma_n} (\rho \boldsymbol{q}) \cdot d\boldsymbol{A} - \int_{\Omega_n} Q \, dV \tag{14}$$

The discretized form of the left hand side term and first term on the right hand side of equation (14) are approximated as:

$$\frac{\partial}{\partial t} \int_{\Omega_n} (\phi s_w \rho) \, dV \approx \left(\frac{d}{dt} (\phi s_w \rho) \right) V_n \tag{15}$$

$$\int_{\Gamma_n} (\rho \boldsymbol{q}) \cdot d\boldsymbol{A} \approx \sum_{n'} (\rho \boldsymbol{q})_{nn'} \cdot \boldsymbol{A}_{nn'} \tag{16}$$

where $\boldsymbol{A}_{nn'}$ [m^2] is the common face area between the n-th and n'-th control volumes. After substituting equations (15) and (16) in equation (14), the resulting ordinary differential equation for the variably saturated flow model is

$$\left(\frac{d}{dt} (\phi s_w \rho) \right) V_n = - \sum_{n'} (\rho \boldsymbol{q})_{nn'} \cdot \boldsymbol{A}_{nn'} - Q_n V_n \tag{17}$$

We perform temporal integration of equation (17) using the backward-Euler scheme:

$$\left(\frac{(\phi s_w \rho)_n^{t+1} - (\phi s_w \rho)_n^{t}}{\Delta t} \right) V_n = - \sum_{n'} (\rho \boldsymbol{q})_{nn'}^{t+1} \cdot \boldsymbol{A}_{nn'} - Q_n^{t+1} V_n \tag{18}$$

Rearranging terms of equation (18) results in a nonlinear equation for the unknown pressure at timestep $t + 1$ as

$$\left(\frac{(\phi s_w \rho)_n^{t+1} - (\phi s_w \rho)_n^{t}}{\Delta t} \right) V_n + \sum_{n'} (\rho \boldsymbol{q})_{nn'}^{t+1} \cdot \boldsymbol{A}_{nn'} + Q_n^{t+1} V_n = 0 \tag{19}$$

In this work, we find the solution to the nonlinear system of equations given by equation (19) using Newton's method via the Scalable Nonlinear Equations Solver (SNES) within the Portable, Extensible Toolkit for Scientific Computing (PETSc)

234   library (Balay et al., 2016). PETSc provides a suite of data structures and routines for

235   the scalable solution of partial differential equations. VSFM uses the composable data

236   management (DMComposite) provided by PETSc (Brown et al., 2012), which enables

237   the potential future application of the model to solve tightly coupled multi-

238   component, multi-physics processes as discussed in section 3.4. A Smooth

239   approximation of the Brooks and Corey (1964) (SBC) water retention curve was

240   developed to facilitate faster convergence of the nonlinear solver (Appendix A).

241   ELMv0 code for subsurface hydrologic processes only supports two vertical mesh

242   configurations and a single set of boundary and source-sink conditions. The

243   monolithic ELMv0 code does not allow for building of code for individual process

244   representations independent of ELMv0 code, thus precluding easy testing of the

245   model against analytical solutions or simulation results from other models. The

246   modular software design of VSFM overcomes ELMv0's software limitation by

247   allowing VSFM code to be built independently of the ELM code. This flexibility of

248   VSFM's build system allows for testing of the VSFM physics in isolation without any

249   influence from the rest of ELM's physics formulations. Additionally, VSFM can be

250   easily configured for a wide range of benchmark problems with different spatial grid

251   resolutions, material properties, boundary conditions, and source-sink forcings.

252   **2.3   VSFM single-column evaluation**

253   We tested the VSFM with three idealized 1-dimensional test problems. First, the

254   widely studied problem for 1D Richards equation of infiltration in dry soil by Celia et

255   al. (1990) was used. The problem setup consists of a 1.0 m long soil column with a

256   uniform initial pressure of −10.0 m (= 3535.5 Pa). Time invariant boundary

257   conditions applied at the top and bottom of soil column are −0.75 m (= 93989.1 Pa)

258   and −10.0 m (= 3535.5 Pa), respectively. The soil properties for this test are given in

259   Table 1. A vertical discretization of 0.01 m is used in this simulation.

260   Second, we simulated transient one-dimensional vertical infiltration in a two-

261   layered soil system as described in Srivastava and Yeh (1991). The domain consisted

262   of a 2 m tall soil column divided equally in two soil types. Except for soil intrinsic

263   permeability, all other soil properties of the two soil types are the same. The bottom

264   soil is 10 times less permeable than the top (Table1). Unlike Srivastava and Yeh
265   (1991), who used exponential functions of soil liquid pressure to compute hydraulic
266   conductivity and soil saturation, we used Mualem (1976) and van Genuchten (1980)
267   constitutive relationships. Since our choice of constitutive relationships for this setup
268   resulted in absence of an analytical solution, we compared VSFM simulations against
269   PFLOTRAN results. The domain was discretized in 200 control volumes of equal soil
270   thickness. Two scenarios, wetting and drying, were modeled to test the robustness of
271   the VSFM solver robustness. Initial conditions for each scenario included a time
272   invariant boundary condition of 0 m (= 1.01325×10^5 Pa) for the lowest control
273   volume and a constant flux of 0.9 cm hr^{-1} and 0.1 cm hr^{-1} at the soil surface for wetting
274   and drying scenarios, respectively.

275   Third, we compare VSFM and PFLOTRAN predictions for soil under variably
276   saturated conditions. The 1-dimensional 1 m deep soil column was discretized in 100
277   equal thickness control volumes. A hydrostatic initial condition was applied such that
278   water table is 0.5 m below the soil surface. A time invariant flux of 2.5×10^{-5} m s^{-1} is
279   applied at the surface, while the lowest control volume has a boundary condition
280   corresponding to the initial pressure value at the lowest soil layer. The soil properties
281   used in this test are the same as those used in the first evaluation.

282   **2.4   Global Simulations and groundwater depth analysis**

283   We performed global simulations with ELMv1-VSFM at a spatial resolution of
284   1.9^0 (latitude) × 2.5^0 (longitude) with a 30 [min] time-step for 200 years, including a
285   180 year spinup and the last 20 years for analysis. The simulations were driven by
286   CRUNCEP meteorological forcing from 1991-2010 (Piao et al., 2012) and configured
287   to use prescribed satellite phenology.

288   For evaluation and calibration, we used the Fan et al. (2013) global ~1 km
289   horizontal resolution WTD dataset (hereafter F2013 dataset), which is based on a
290   combination of observations and hydrologic modeling. We aggregated the dataset to
291   the ELMv1-VSFM spatial resolution. ELM-VSFM's default vertical soil discretization
292   uses 15 soil layers to a depth of ~42 m, with an exponentially varying soil thickness.
293   However, ~13% of F2013 land gridcells have a water table deeper than 42 m. We

294   therefore modified ELMv1-VSFM to extend the soil column to a depth of 150 m with

295   59 soil layers; the first nine soil layer thicknesses were the same as described in

296   Oleson (2013) and the remaining layers (10-59) were set to a thickness of 3 m.

297   **2.5   Estimation of the subsurface drainage parameterization**

298   In the VSFM formulation, the dominant control on long-term GW depth is the

299   subsurface drainage flux, q_d [kg m^{-2} s^{-1}], which is calculated based on water table

300   depth, z_∇[m], (Niu et al. (2005)):

$$q_d = q_{d,max} exp(-f_d z_\nabla) \tag{20}$$

301   where $q_{d,max}$ [kg m^{-2} s^{-1}] is the maximum drainage flux that depends on gridcell slope

302   and f_d [m^{-1}] is an empirically-derived parameter. The subsurface drainage flux

303   formulation of Niu et al. (2005) is similar to the TOPMODEL formulation (Beven and

304   Kirkby, 1979) and assumes the water table is parallel to the soil surface. While

305   Sivapalan et al. (1987) derived $q_{d,max}$ as a function of lateral hydraulic anisotropy,

306   hydraulic conductivity, topographic index, and decay factor controlling vertical

307   saturated hydraulic conductivity, Niu et al. (2005) defined $q_{d,max}$ as a single

308   calibration parameter. ELMv0 uses $f_d = 2.5$ m^{-1} as a global constant and estimates

309   maximum drainage flux when WTD is at the surface as $q_{d,max} = 10 \sin(\beta)$ kg m^{-2} s^{-1},

310   where β [radians] is mean grid cell topographic slope. Of the two parameters, f_d and

311    $q_{d,max}$, available for model calibration, we choose to calibrate f_d because the

312   uncertainty analysis by Hou et al. (2012) identified it as the most significant

313   hydrologic parameter in CLM4. To improve on the f_d parameter values, we

314   performed an ensemble of global simulations with f_d values of 0.1, 0.2, 0.5, 1.0, 2.5,

315   5.0, 10.0, and 20 m^{-1}. Each ensemble simulation was run for 200 years to ensure an

316   equilibrium solution, and the last 20 years were used for analysis. A non-linear

317   functional relationship between f_d and WTD was developed for each gridcell and

318   then the F2013 dataset was used to estimate an optimal f_d for each gridcell.

319   **2.6   Global ELM-VSFM evaluation**

320   With the optimal f_d values, we ran a ELM-VSFM simulation using the protocol

321   described above. We then used the International Land Model Benchmarking package

322   (ILAMB) to evaluate the ELMv1-VSFM predictions of surface energy budget, total
323   water storage anomalies (TWSA), and river discharge (Collier et al., 2018; Hoffman et
324   al., 2017). ILAMB evaluates model prediction bias, RMSE, and seasonal and diurnal
325   phasing against multiple observations of energy, water, and carbon cycles at in-situ,
326   regional, and global scales. Since ELM-VSFM simulations in this study did not include
327   an active carbon cycle, we used the following ILAMB benchmarks for water and
328   energy cycles: (i) latent and surface energy fluxes using site-level measurements from
329   FLUXNET (Lasslop et al., 2010) and globally from FLUXNET-MTE (Jung et al., 2009));
330   (ii) terrestrial water storage anomaly (TWSA) from the Gravity Recovery And Climate
331   Experiment (GRACE) observations (Kim et al., 2009); and (iii) stream flow for the 50
332   largest global river basins (Dai and Trenberth, 2002). We applied ILAMB benchmarks
333   for ELMv1-VSFM simulations with default and calibrated f_d to ensure improvements
334   in WTD predictions did not degrade model skill for other processes.

335   **3   Results and discussion**

336   **3.1   VSFM single-column evaluation**

337   For the 1D Richards equation infiltration in dry soil comparison, we evaluated
338   the solutions at 24-hr against those published by Celia et al. (1990) (Figure 1). The
339   VSFM solver accurately represented the sharp wetting front over time, where soil
340   hydraulic properties change dramatically due to non-linearity in the soil water
341   retention curve.
342   For the model evaluation of infiltration and drying in layered soil, the results of
343   the VSFM and PFLOTRAN are essentially identical. In both models and scenarios, the
344   higher permeability top soil responds rapidly to changes in the top boundary
345   condition and the wetting and drying fronts progressively travel through the less
346   permeable soil layer until soil liquid pressure in the entire column reaches a new
347   steady state by about 100 h (Figure 2).
348   We also evaluated the VSFM predicted water table dynamics against PFLOTRAN
349   predictions from an initial condition of saturated soil below 0.5 m depth. The
350   simulated water table rises to 0.3 m depth by 1 day and reaches the surface by 2 days,

351   and the VSFM and PFLOTRAN predictions are essentially identical Figure 3. Soil
352   properties, spatial discretization, and timestep used for the three single-column
353   problems are summarized in Table 1 These three evaluation simulations demonstrate
354   the VSFM accurately represents soil moisture dynamics under conditions relevant to
355   ESM-scale prediction.

3.2   Subsurface drainage parameterization estimation

357   The simulated nonlinear WTD-f_d relationship is a result of the subsurface
358   drainage parameterization flux given by equation (20) (Figure 4(a) and (b)). For
359   $0.1 \leq f_d \leq 1$, the slope of the WTD-f_d relationship for all gridcells is log-log linear
360   with a slope of -1.0 ± 0.1. The log-log linear relationship breaks down for $f_d > 1$,
361   where the drainage flux becomes much smaller than infiltration and
362   evapotranspiration (Figure 4(c) and (d)). Thus, at larger f_d, the steady state z_∇
363   becomes independent of f_d and is determined by the balance of infiltration and
364   evapotranspiration.

365   For 79% of the global gridcells, the ensemble range of simulated WTD spanned
366   the F2013 dataset. The optimal value of f_d for each of these gridcells was obtained by
367   linear interpolation in the log-log space (e.g., Figure 4 (a)). For the remaining 21% of
368   gridcells where the shallowest simulated WTD across the range of f_d was deeper than
369   that in the F2013 dataset, the optimal f_d value was chosen as the one that resulted in
370   the lowest absolute WTD error (e.g., Figure 4 (b)). At large f_d values, the drainage flux
371   has negligible effects on WTD, yet simulated WTD is not sufficiently shallow to match
372   the F2013 observations, which indicates that either evapotranspiration is too large
373   or infiltration is too small. There was no difference in the mean percentage of sand
374   and clay content between grids cells with and without an optimal f_d value. The
375   optimal f_d has a global average of 1.60 m^{-1} $\pm$ 2.68 m^{-1} and 72% of global gridcells have
376   an optimal f_d value lower than the global average (Figure 5).

3.3   Global simulation evaluation

378   The ELMv1-VSFM predictions are much closer to the F2013 dataset (Figure 6a)
379   using optimal globally-distributed f_d values (Figure 6c) compared to the default f_d

380 value (Figure 6b). The significant reduction in WTD bias (model – observation) is
381 mostly due to improvement in the model's ability to accurately predict deep WTD
382 using optimal f_d values. In the simulation using optimal globally-distributed f_d
383 values, all gridcells with WTD bias > 3.7 m were those for which an optimal f_d was
384 not found. The mean global bias, RMSE, and R^2 values improved in the new ELMv1-
385 VSFM compared to the default model (Table 2). The 79% of global grid cells for which
386 an optimal f_d value was estimated had significantly better water table prediction
387 with a bias, RMSE, and R^2 of -0.04 m, 0.67 m, and 0.99, respectively, as compared to
388 the remaining 21% of global gridcells that had a bias, RMSE, and R^2 of -9.82 m, 18.08
389 m, and 0.31, respectively. The simulated annual WTD range, which we define to be
390 the difference between maximum and minimum WTD in a year, has a spatial mean
391 and standard deviation of 0.32 m and 0.58 m, respectively, using optimal f_d values
392 (Figure 7 (a)). The annual WTD range decreased by 0.24 m for the 79% of the grid
393 cells for which an optimal f_d value was estimated (Figure 7 (b)).

394   Globally-averaged WTD in ELMv1-VSFM simulations with default f_d and
395 optimal f_d values were 10.5 m and 20.1 m, respectively. Accurate prediction of deep
396 WTD in the simulation with optimal f_d caused very small differences in near-surface
397 soil moisture (Figure 8). The 79% of grid cells with an optimal f_d value had deeper
398 globally-averaged WTDs than when using the default f_d value (24.3 m vs. 8.6 m). For
399 these 79% of grid cells, the WTD was originally deep enough to not impact near-
400 surface conditions (Kollet and Maxwell, 2008); therefore, further lowering of WTD
401 led to negligible changes in near-surface hydrological conditions.

402   The International Land Model Benchmarking (ILAMB) package (Hoffman et al.,
403 2017) provides a comprehensive evaluation of predictions of carbon cycle states and
404 fluxes, hydrology, surface energy budgets, and functional relationships by
405 comparison to a wide range of observations. We used ILAMB to evaluate the
406 hydrologic and surface energy budget predictions from the new ELMv1-VSFM model
407 (Table 3). Optimal f_d values had inconsequential impacts on simulated surface
408 energy fluxes at site-level and global scales. Optimal f_d values led to improvement in
409 prediction of deep WTD (with a mean value of 24.3 m) for grid cells that had an
410 average WTD of 8.7 m in the simulation using default f_d values. Thus, negligible

differences in surface energy fluxes between the two simulations are consistent with the findings of Kollet and Maxwell (2008), who identified decoupling of groundwater dynamics and surface processes at a WTD of ~10 m. There were slight changes in bias and RMSE for predicted TWSA, but the ILAMB score remained unchanged. The TWSA amplitude is lower for the simulation with optimal f_d values, consistent with the associated decrease in annual WTD range. ELM's skill in simulating runoff for the 50 largest global watersheds remained unchanged. Two additional 10-years long simulations were performed to investigate the sensitivity of VSFM simulated WTD to spatial and temporal discretization. Results show that simulated WTD is insensitive to temporal discretization, and has small sensitivity to vertical spatial resolution. See supplementary material for details regarding setup and analysis of results from the two additional simulations.

Finally, we evaluated the computational costs of implementing VSFM in ELM and compared them to the default model. We performed 5-year long simulations for default and VSFM using 96, 192, 384, 768, and 1536 cores on the Edison supercomputer at the National Energy Research Scientific Computing Center. Using an optimal processor layout, we found that ELMv1-VSFM is ~30% more expensive than the default ELMv1 model (Supplementary material Fig S 1). We note that the relative computational cost of the land model in a fully coupled global model simulation is generally very low. Dennis et al. (2012) reported computational cost of the land model to be less than 1% in ultra-high-resolution CESM simulations. We therefore believe that the additional benefits associated with the VSFM formulation are well justified by this modest increase in computational cost. In particular, VSFM allows a greater variety of mesh configurations and boundary conditions, and can accurately simulate WTD for the ~13% of global grid cells that have a water table deeper than 42 [m] (Fan et al. (2013).

3.4   Caveats and Future Work

The significant improvement in WTD prediction using optimal f_d values demonstrates VSFM's capabilities to model hydrologic processes using a unified physics formulation for unsaturated-saturated zones. However, several caveats

441 remain due to uncertainties in model structure, model parameterizations, and climate
442 forcing data.

443   In this study, we assumed a spatially homogeneous depth to bedrock (DTB) of
444 150 m. Recently, Brunke et al. (2016) incorporated a global ~1 km dataset of soil
445 thickness and sedimentary deposits (Pelletier et al., 2016) in CLM4.5 to study the
446 impacts of soil thickness spatial heterogeneity on simulated hydrological and thermal
447 processes. While inclusion of heterogeneous DTB in CLM4.5 added more realism to
448 the simulation setup, no significant changes in simulated hydrologic and energy
449 fluxes were reported by Brunke et al. (2016). Presently, work is ongoing in the E3SM
450 project to include variable DTB within ELM and future simulations will examine the
451 impact of those changes on VSFM's prediction of WTD. Our use of the 'satellite
452 phenology' mode, which prescribes transient LAI profiles for each plant functional
453 type in the gridcell, ignored the likely influence of water cycle dynamics and nutrient
454 constraints on the C cycle (Ghimire et al., 2016; Zhu et al., 2016). Estimation of soil
455 hydraulic properties based on soil texture data is critical for accurate LSM predictions
456 (Gutmann and Small, 2005) and this study does not account for uncertainty in soil
457 hydraulic properties.

458   Lateral water redistribution impacts soil moisture dynamics (Bernhardt et al.,
459 2012), biogeochemical processes in the root zone (Grant et al., 2015), distribution of
460 vegetation structure (Hwang et al., 2012), and land-atmosphere interactions (Chen
461 and Kumar, 2001; Rihani et al., 2010). The ELMv1-VSFM developed in this study does
462 not include lateral water redistribution between soil columns and only simulates
463 vertical water transport. Lateral subsurface processes can be included in LSMs via a
464 range of numerical discretization approaches of varying complexity, e.g., adding
465 lateral water as source/sink terms in the 1D model, implementing an operator split
466 approach to solve vertical and lateral processes in a non-iterative approach (Ji et al.,
467 2017), or solving a fully coupled 3D model (Bisht et al., 2017; Bisht et al., 2018; Kollet
468 and Maxwell, 2008). Additionally, lateral transport of water can be implemented in
469 LSMs at a subgrid level (Milly et al., 2014) or grid cell level (Miguez-Macho et al.,
470 2007). The current implementation of VSFM is such that each processor solves the
471 variably saturated Richards equation for all independent soil columns as one single

472   problem. Thus, extension of VSFM to solve the tightly coupled 3D Richards equation

473   on each processor locally while accounting for lateral transport of water within grid

474   cells and among grid cells is straightforward. The current VSFM implementation can

475   also be easily extended to account for subsurface transport of water among grid cells

476   that are distributed across multiple processors by modeling lateral flow as

477   source/sink terms in the 1D model. Tradeoffs between approaches to represent

478   lateral processes and computational costs need to be carefully studied before

479   developing quasi or fully three-dimensional land surface models (Clark et al., 2015).

480   Transport of water across multiple components of the Soil Plant Atmosphere

481   Continuum (SPAC) has been identified as a critical process in understanding the

482   impact of climate warming on the global carbon cycle (McDowell and Allen, 2015).

483   Several SPAC models have been developed by the ecohydrology community and

484   applied to study site-level processes (Amenu and Kumar, 2008; Bohrer et al., 2005;

485   Manoli et al., 2014; Sperry et al., 1998), yet implementation of SPAC models in global

486   LSMs is limited (Clark et al., 2015). Similarly, current generation LSMs routinely

487   ignore advective heat transport within the subsurface, which has been shown to be

488   important in high-latitude environments by multiple field and modeling studies

489   (Bense et al., 2012; Frampton et al., 2011; Grant et al., 2017; Kane et al., 2001). The

490   use of PETSc's DMComposite in VSFM provides flexibility for solving a tightly coupled

491   multi-component problem (e.g., transport of water through the soil-plant continuum)

492   and multi-physics problem (e.g., fully coupled conservation of mass and energy

493   equations in the subsurface). DMComposite allows for an easy assembly of a tightly

494   coupled multi-physics problem from individual physics formulations (Brown et al.,

495   2012).

496   **4   Summary and Conclusion**

497   Starting from the climate-scale land model ELMv0, we incorporated a unified

498   physics formulation to represent soil moisture and groundwater dynamics that are

499   solved using PETSc. Application of VSFM to three benchmarks problems

500   demonstrated its robustness to simulated subsurface hydrologic processes in

501   coupled unsaturated and saturated zones. Ensemble global simulations at $1.9^0 \times 2.5^0$

502   were performed for 200 years to obtain spatially heterogeneous estimates of the

503   subsurface drainage parameter, f_d, that minimized mismatches between predicted

504   and observed WTDs. In order to simulate the deepest water table reported in the Fan

505   et al. (2013) dataset, we used 59 vertical soil layers that reached a depth of 150 m.

506   An optimal f_d was obtained for 79% of the grids cells in the domain. For the

507   remaining 21% of grid cells, simulated WTD always remained deeper than observed.

508   Calibration of f_d significantly improved global WTD prediction by reducing bias and

509   RMSE and increasing R^2. Grids without an optimal f_d were the largest contributor of

510   error in WTD predication. ILAMB benchmarks on simulations with default and

511   optimal f_d showed negligible changes to surface energy fluxes, TWSA, and runoff.

512   ILAMB metrics ensured that model skill was not adversely impacted for all other

513   processes when optimal f_d values were used to improve WTD prediction.

514

5   Appendix

5.1   Smooth approximation of Brooks-Corey water retention curve

517   The Brooks and Corey (1964) water retention curve of equation (10) has a

518   discontinuous derivative at $P = P_c^0$. Figure A 1 illustrates an example. To improve

519   convergence of the nonlinear solver at small capillary pressures, the smoothed

520   Brooks-Corey function introduces a cubic polynomial, $B(P_c)$, in the neighborhood of

521   P_c^0.

$$s_e = \begin{cases} (-\alpha P_c)^{-\lambda} & if\ P_c \leq P_u \\ B(P_c) & if\ P_u < P_c < P_s \\ 1 & if\ P_s \leq P_s \end{cases} \tag{21}$$

522   where the breakpoints P_u and P_s satisfy $P_u < P_c^0 < P_s \leq 0$. The smoothing

523   polynomial

$$B(P_c) = b_0 + b_1(P_c - P_s) + b_2(P_c - P_s)^2 + b_3(P_c - P_s)^3 \tag{22}$$

524   introduces four more parameters, whose values follow from continuity. In particular

525   matching the saturated region requires $B(P_s) = b_0 = 1$, and a continuous derivative

526 at $P_c = P_s$ requires $B'(P_s) = b_1 = 0$. Similarly, matching the value and derivative at

527 $P_c = P_u$ requires

$$b_2 = \frac{-1}{\Delta^2}\left[3 - (\alpha P_u)^{-\lambda}\left(3 + \frac{\lambda\Delta}{P_u}\right)\right] \tag{23}$$

$$b_3 = \frac{-1}{\Delta^3}\left[2 - (\alpha P_u)^{-\lambda}\left(2 + \frac{\lambda\Delta}{P_u}\right)\right] \tag{24}$$

528 where $\Delta = P_u - P_s$. Note $P_u \leq \Delta < 0$.

529   In practice, setting P_u too close to P_c^0 can produce an unwanted local maximum

530 in the cubic smoothing regime, resulting in se > 1. Avoiding this condition requires

531 that $B(P_c)$ increase monotonically from $P_c = P_u$, where $B'(P_c) > 0$, to $P_c = P_s$, where

532 $B'(P_c) = 0$. Thus a satisfactory pair of breakpoints ensures

$$B'(P_c) = [P_c - P_s][2b_2 + 3b_3(P_c - P_s)] > 0 \tag{25}$$

533 throughout $P_u \leq P_c < P_s$.

534   Let P_c^* denote a local extremum of B, so that $B'(P_c^*) = 0$. If $P_c^* \neq P_s$, it follows

535 $P_c^* - P_s = -2b_2/(3b_3)$. Rewriting equation 22, $B'(P_c) = (P_c - P_s)3b_3(P_c - P_c^*)$ shows

536 that $B'(P_c^*) > 0$ requires either: (1) $b_3 < 0$ and $P_c^* < P_u$; or (2) $b_3 > 0$ and $P_c^* > P_u$;.

537 The first possibility places P_c^* outside the cubic smoothing regime, and so does not

538 constrain the choice of P_u or P_s. The second possibility allows an unwanted local

539 extremum at $P_u < P_c^* < P_s$. In this case, $b_3 > 0$ implies $b_2 < 0$ (since $P_c^* < P_s \leq 0$).

540 Then since $B''(P_c^*) = -2b_2$, the local extremum is a maximum, resulting in $s_e(P_c^*) >$

541 1.

542   Given a breakpoint P_s, one strategy for choosing P_u is to guess a value, then

543 check whether the resulting b_2 and b_3 produces $P_u < P_c^* < P_s$. If so, P_u should be

544 made more negative. An alternative strategy is to choose P_u in order the guarantee

545 acceptable values for b_2 and b_3. One convenient choice forces $b_2 = 0$. Another picks

546 P_u in order to force $b_3 = 0$. Both of these reductions: (1) ensure $B(P_c)$ has a positive

547 slope throughout the smoothing interval; (2) slightly reduce the computation cost of

548 finding $s_e(P_c)$ for P_c on the smoothing interval; and (3) significantly reduce the

549 computational cost of inverting the model, in order to find P_c as a function of s_e.

550   As shown in Figure A 1, the two reductions differ mainly in that setting $b_2 = 0$

551 seems to produce narrower smoothing regions (probably due to the fact that this

552   choice gives zero curvature at $P_c = P_s$, while $b_3 = 0$ yields a negative second
553   derivative there). However, we have not verified this observation analytically.

554   Both reductions require solving a nonlinear expression either equation (23) or
555   (24), for P_u. While details are beyond the scope of this paper, we note that we have
556   used a bracketed Newton-Raphson's method. The search switches to bisection when
557   Newton-Raphson would jump outside the bounds established by previous iterations,
558   and by the requirement $P_u < P_c^0$ In any event, since the result of this calculation may
559   be cached for use throughout the simulation, it need not be particularly efficient.

5.2   Residual equation of VSFM formulation

561   The residual equation for the VSFM formulation at $t + 1$ time level for n-th control
562   volume is given by

$$R_n^{t+1} \equiv \left(\frac{(\phi s_w \rho)_n^{t+1} - (\phi s_w \rho)_n^t}{\Delta t} \right) V_n + \sum_{n'} (\rho \boldsymbol{q})_{nn'}^{t+1} \cdot \boldsymbol{A}_{nn'} + Q_n^{t+1} V_n = 0 \qquad (26)$$

563   where ϕ [mm³ mm³] is the soil porosity, s_w [-] is saturation, ρ [kg m⁻³] is water
564   density, $\vec{q}_{nn'}$ [m s⁻¹] is the Darcy flow velocity between n-th and n'-th control
565   volumes, $A_{nn'}$ [m s⁻¹] is the interface face area between n-th and n'-th control
566   volumes Q [kg m⁻³ s⁻¹] is a sink of water. The Darcy velocity is computed as

$$\boldsymbol{q}_{nn'} = -\left(\frac{k k_r}{\mu} \right)_{nn'} \left[\frac{P_{n'} - P_n - \rho_{nn'}(\boldsymbol{g} \cdot \boldsymbol{d}_{nn'})}{d_n + d_{n'}} \right] \boldsymbol{n}_{nn'} \qquad (27)$$

567   where κ [m⁻²] is intrinsic permeability, κ_r [-] is relative permeability, μ [Pa s] is
568   viscosity of water, P [Pa] is pressure], $\boldsymbol{g}$ [m s⁻²] is the acceleration due to gravity,
569   d_n [m] and $d_{n'}$ [m] is distance between centroid of n-th and n'-th control volume to
570   the common interface between the two control volumes, $\boldsymbol{d}_{nn'}$ is a distance vector
571   joining centroid of n-th and n'-th control volume, and $\boldsymbol{n}_{nn'}$ is a unit normal vector
572   joining centroid of n-th and n'-th control volume.

573   The density at the interface of control volume, $\rho_{nn'}$, is computed as inverse
574   distance weighted average by

$$\rho_{nn'} = \omega_{n'} \rho_n + \omega_n \rho_{n'} \qquad (28)$$

575   where ω_n and $\omega_{n'}$ are given by

$$\omega_n = \frac{d_n}{d_n + d_{n'}} = (1 - \omega_{n'}) \tag{29}$$

576 The first term on the RHS of equation 27 is computed as the product of distance

577 weighted harmonic average of intrinsic permeability, $k_{nn'}$, and upwinding of

578 k_r/μ $(= \lambda)$ as

$$\left(\frac{kk_r}{\mu}\right)_{nn'} = k_{nn'}\left(\frac{k_r}{\mu}\right)_{nn'} = \left[\frac{k_n k_{n'}(d_n + d_{n'})}{k_n d_{n'} + k_{n'} d_n}\right]\lambda_{nn'} \tag{30}$$

579 where

$$\lambda_{nn'} = \begin{cases} (k_r/\mu)_n & if \ \vec{q}_{nn'} > 0 \\ (k_r/\mu)_{n'} & otherwise \end{cases} \tag{31}$$

580 By substituting equation 28, 29 and 30 in equation 27, we obtain

$$\boldsymbol{q}_{nn'} = -\left[\frac{k_n k_{n'}}{k_n d_{n'} + k_{n'} d_n}\right]\lambda_{nn'}[P_{n'} - P_n - \rho_{nn'}(\boldsymbol{g}.\boldsymbol{d}_{nn'})]\boldsymbol{n}_{nn'} \tag{32}$$

581

5.3 Jacobian equation of VSFM formulation

583 The discretized equations of VSFM leads to a system of nonlinear equations given by

584 $\boldsymbol{R}^{t+1}(\boldsymbol{P}^{t+1}) = \boldsymbol{0}$, which are solved using Newton's method using the Portable,

585 Extensible Toolkit for Scientific Computing (PETSc) library. The algorithm of

586 Newton's method requires solution of the following linear problem

$$\boldsymbol{J}^{t+1,k}(\boldsymbol{P}^{t+1,k})\,\Delta\boldsymbol{P}^{t+1,k} = -\boldsymbol{R}^{t+1,k}(\boldsymbol{P}^{t+1,k}) \tag{33}$$

587 where $\boldsymbol{J}^{t+1,k}(\boldsymbol{P}^{t+1,k})$ is the Jacobian matrix. In VSFM, the Jacobian matrix is

588 computed analytically. The contribution to the diagonal and off-diagonal entry of the

589 Jacobian matrix from n-th residual equations are given by

$$J_{nn} = \frac{\partial R_n}{\partial P_n} = \left(\frac{V_n}{\Delta t}\right)\frac{\partial(\rho\phi s_w)}{\partial P_n} + \sum_{n'}\frac{\partial(\rho\boldsymbol{q})_{nn'}}{\partial P_n}\,A_{nn'} + \frac{\partial Q_n^{t+1}}{\partial P_n}V_n \tag{34}$$

$$J_{nn'} = \frac{\partial R_n}{\partial P_{n'}} = \sum_{n'}\frac{\partial(\rho\boldsymbol{q})_{nn'}}{\partial P_{n'}}\,A_{nn'} + \frac{\partial Q_n^{t+1}}{\partial P_{n'}}V_n \tag{35}$$

590 The derivative of the accumulation term in J_{nn} is computed as

$$\frac{\partial(\rho\phi s_w)}{\partial P_n} = \phi s_w\frac{\partial\rho}{\partial P_n} + \rho s_w\frac{\partial\phi}{\partial P_n} + \rho\phi\frac{\partial s_w}{\partial P_n} \tag{36}$$

591 The derivative of flux between n-th and n'-th control volume with respect to
592 pressure of each control volume is given as

$$\frac{\partial(\rho\boldsymbol{q})_{nn'}}{\partial P_n} = \rho_{nn'}\frac{\partial\boldsymbol{q}_{nn'}}{\partial P_n} + \boldsymbol{q}_{nn'}\omega_n\frac{\partial\rho_n}{\partial P_n} \tag{37}$$

593

$$\frac{\partial(\rho\boldsymbol{q})_{nn'}}{\partial P_{n'}} = \rho_{nn'}\frac{\partial\boldsymbol{q}_{nn'}}{\partial P_{n'}} + \boldsymbol{q}_{nn'}\omega_{n'}\frac{\partial\rho_{n'}}{\partial P_{n'}} \tag{38}$$

594 Lastly, the derivative of Darcy velocity between n-th and n'-th control volume with
595 respect to pressure of each control volume is given as

$$\frac{\partial\boldsymbol{q}_{nn'}}{\partial P_n} = \left[\frac{k_n k_{n'}}{k_n d_{n'} + k_{n'} d_n}\right]\lambda_{nn'}\left[1 + \omega_n(\boldsymbol{g}.\boldsymbol{d}_{nn'})\frac{\partial\rho_n}{\partial P_n}\right]\boldsymbol{n}_{nn'} + \boldsymbol{q}_{nn'}\frac{\partial\big(ln(\lambda_{nn'})\big)}{\partial P_n} \tag{39}$$

$$\frac{\partial\boldsymbol{q}_{nn'}}{\partial P_{n'}} = \left[\frac{k_n k_{n'}}{k_n d_{n'} + k_{n'} d_n}\right]\lambda_{nn'}\left[-1 + \omega_n(\boldsymbol{g}.\boldsymbol{d}_{nn'})\frac{\partial\rho_{n'}}{\partial P_{n'}}\right]\boldsymbol{n}_{nn'}$$
$$+ \boldsymbol{q}_{nn'}\frac{\partial\big(ln(\lambda_{nn'})\big)}{\partial P_{n'}} \tag{40}$$

596 ## 5.4 Numerical checks in VSFM

597 VSFM uses a two-stage check to determine an acceptable numerical
598 solution:

599 Stage-1: At any temporal integration stage, the model attempts to solve
600 the set of nonlinear equations given by Equation (19) with a given
601 timestep. If the model fails to find a solution to the nonlinear equations
602 with a given error tolerance settings, the timestep is reduced by half and
603 the model again attempts to solve the nonlinear problem. If the model
604 fails to find a solution after a maximum number of time step cuts
605 (currently 20), the model reports an error and stops execution. None of
606 the simulations reported in this paper failed this check.

607 Stage-2: After a numerical solution for the nonlinear problem is obtained,
608 a mass balance error is calculated as the difference between input and

609 output fluxes and change in mass over the integration timestep. If the

610 mass balance error exceeds 10-5 kg m-2, the error tolerances for the

611 nonlinear problem are tightened by a factor of 10 and the model re-enters

612 Stage-1. If the model fails to find a solution with an acceptable mass

613 balance error after 10 attempts of tightening error tolerances, the model

614 reports an error and stops execution. None of the simulations reported in

615 this paper failed this check.

6 Code availability

617 The standalone VSFM code is available at https://github.com/MPP-LSM/MPP and the

618 DOI for the code is https://doi.org/10.5281/zenodo.1412949. Notes on how to run

619 the VSFM for all benchmark problems and compare results against PFLOTRAN at

620 https://bitbucket.org/gbisht/notes-for-gmd-2018-44.

621 The research was performed using E3SM v1.0 and the code is available at

622 https://github.com/E3SM-Project/E3SM.

7 Competing interests

624 The authors declare that they have no conflict of interest.

625

8 Acknowledgements

627 This research was supported by the Director, Office of Science, Office of Biological

628 and Environmental Research of the US Department of Energy under contract no. DE-

629 AC02-05CH11231 as part of the Energy Exascale Earth System Model (E3SM)

630 programs.

631

9 Tables

Table 1 Soil properties and discretization used in the three test problems described in section 2.3.

Problem number	ϕ [-]	m [-]	α [Pa^{-1}]	k [m^2]	dz [m]	dt [s]
1	0.368	0.5	3.4257x10^{-4}	8.3913x10^{-12}	0.001	180
2	0.4	0.5455	4x10^{-4}	2.5281x10^{-12} (top layer) 2.5281x10^{-13} (bottom layer)	0.01	100
3	0.368	0.5	3.4257x10^{-4}	8.3913x10^{-12}	0.01	3600

635

Table 2 Bias, root mean square error (RMSE), and correlation (R^2) between simulated water table depth and Fan et al. (2013) data.

	Bias [m]	RMSE [m]	R^2
For all grids in ELM simulation with default f_{drain}	-10.3	21.3	0.28
For all grids in ELM simulation with optimal f_{drain}	2.10	8.33	0.91
For 79% grids with optimal f_{drain} in ELM simulation with optimal f_{drain}	-0.04	0.67	0.99
For 21% grids without optimal f_{drain} in ELM simulation with optimal f_{drain}	-9.82	18.08	0.31

638

639

640 **Table 3 ILAMB benchmark scores for latent heat flux (LH), sensible heat flux**

641 **(SH), total water storage anomaly (TWSA), and surface runoff. The calculation**

642 **of ILAMB metrics and scores are described at http://redwood.ess.uci.edu/.**

	Data Source	**Simulation with default f_d**			**Simulation with optimal f_d**		
		Bias	**RMSE**	**ILAMB Score**	**Bias**	**RMSE**	**ILAMB Score**
LH	FLUXNET	10.1 [Wm^{-2}]	21.0 [Wm^{-2}]	0.68	9.5 [Wm^{-2}]	21.3 [Wm^{-2}]	0.68
	GBAF	7.1 [Wm^{-2}]	16.3 [Wm^{-2}]	0.81	6.3 [Wm^{-2}]	16.3 [Wm^{-2}]	0.81
SH	FLUXNET	6.7 [Wm^{-2}]	22.5 [Wm^{-2}]	0.66	7.1 [Wm^{-2}]	22.8 [Wm^{-2}]	0.65
	GBAF	6.9 [Wm^{-2}]	21.2 [Wm^{-2}]	0.71	7.6 [Wm^{-2}]	21.7 [Wm^{-2}]	0.70
TWSA	GRACE	1.3 [cm]	7.8 [cm]	0.48	3.0 [cm]	9.6 [cm]	0.48
Runoff	Dai	-0.26 [kg $^{m-2}$ d^{-1}]	0.91 [m^{-2}m^{-2} d^{-1}]	0.52	-0.23 [kg m^{-2} d^{-1}]	0.88 [kg m^{-2} d^{-1}]	0.50

643

644

 10 Figures

646
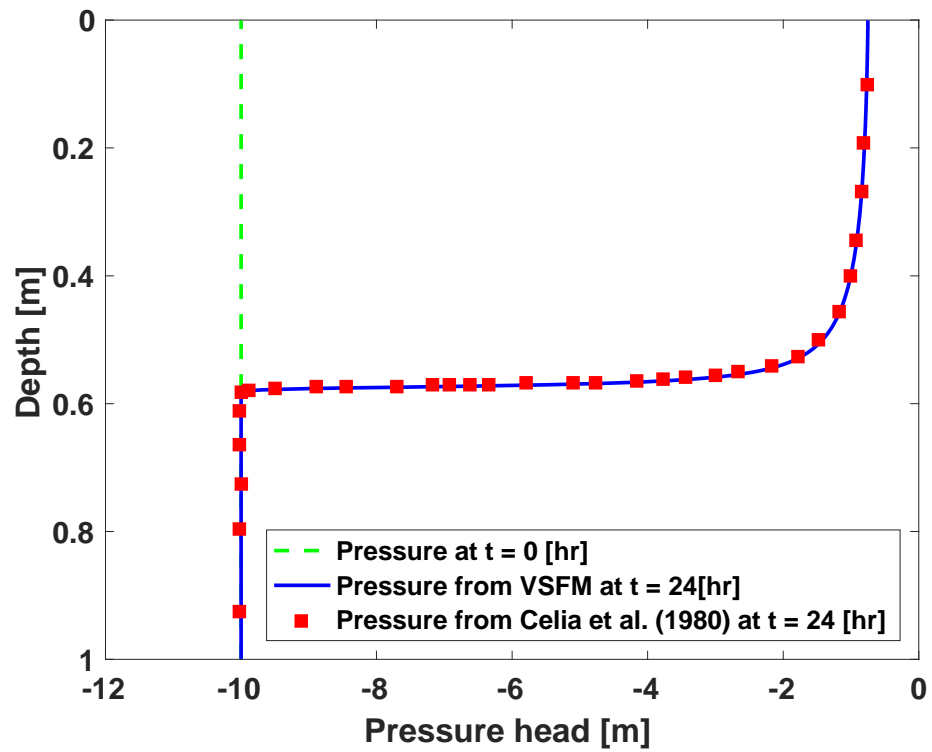
Figure 1. Comparison of VSFM simulated pressure profile (blue line) against data (red square) reported in Celia et al. (1990) at time = 24 hr for infiltration in a dry soil column. Initial pressure condition is shown by green line.

650
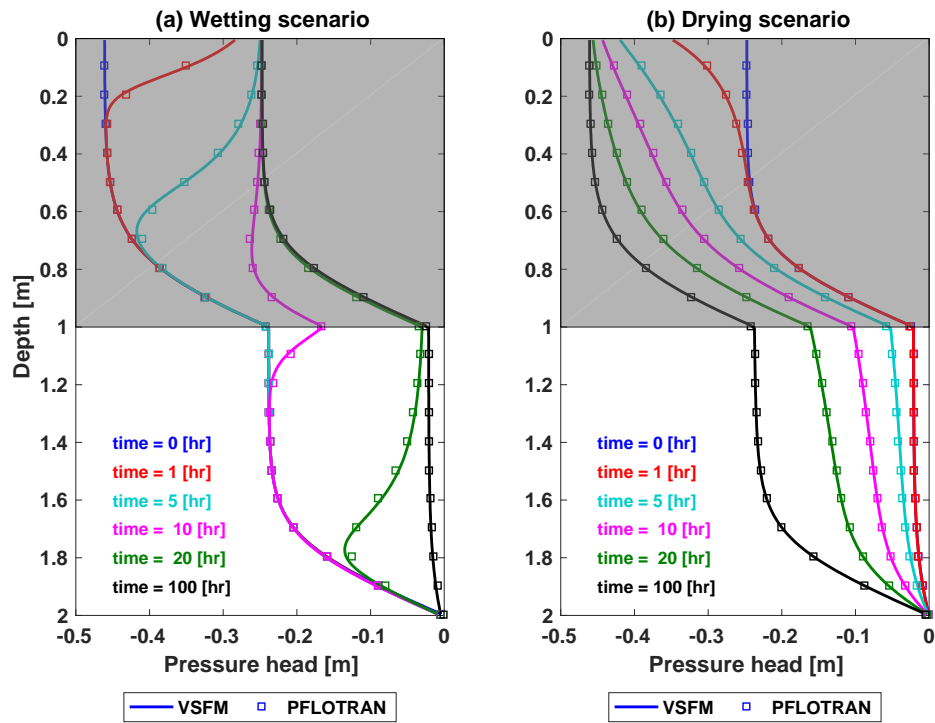
Figure 2. Transient liquid pressure simulated for a two layer soil system by VSFM (solid line) and PFLOTRAN (square) for wetting (left) and drying (right) scenarios.

654
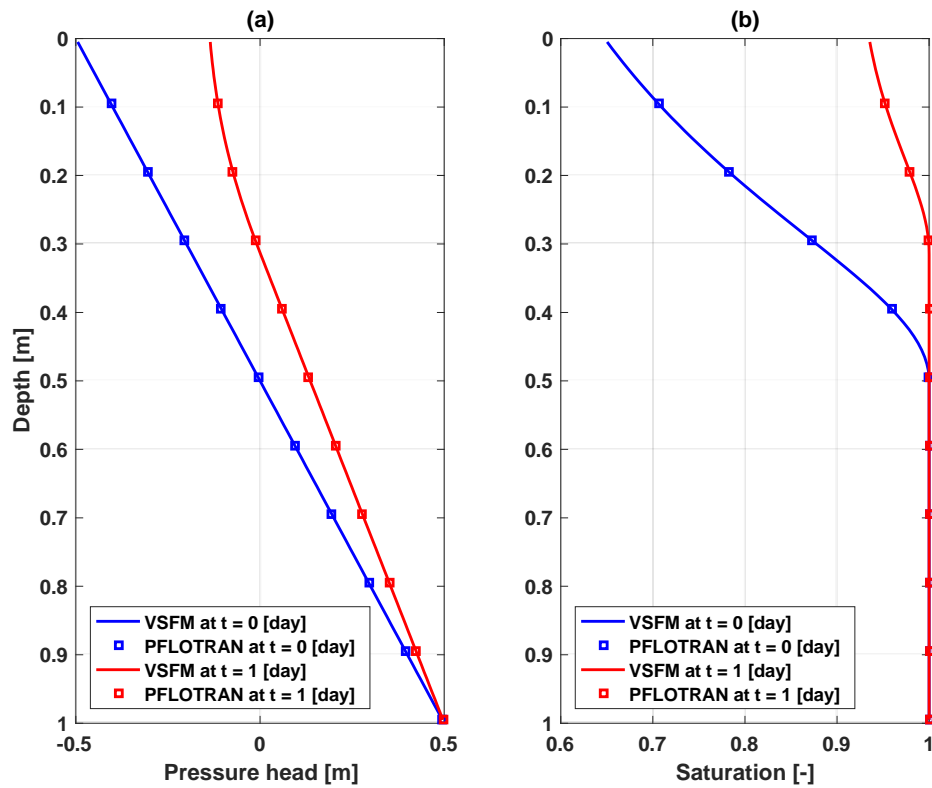
Figure 3. Transient liquid pressure (a) and soil saturation (b) simulated by VSFM (solid line) and PFLOTRAN (square) for the water table dynamics test problem.

658
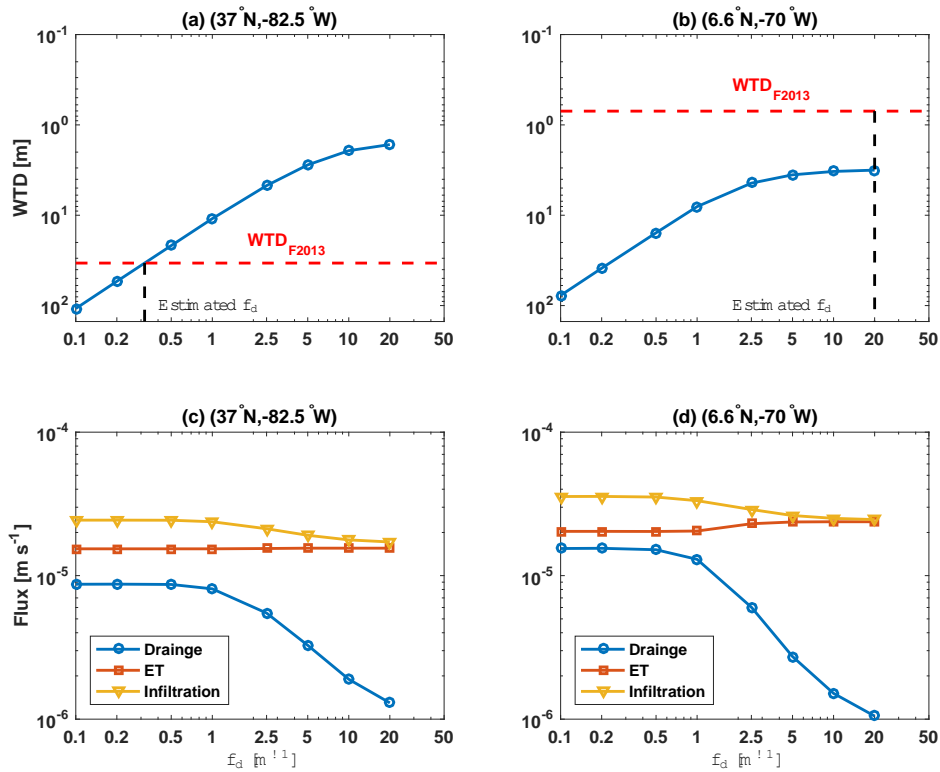
Figure 4. (a-b) The nonlinear relationship between simulated water table depth (WTD) and f_d for two gridcells within ELM's global grid. WTD from the Fan et al. (2013) dataset and optimal f_d for the two gridcells are shown with a dashed red and dashed black lines, respectively. (c-d) The simulated drainage, evapotranspiration, and infiltration fluxes as functions of optimal f_d for the two ELM gridcells.

665
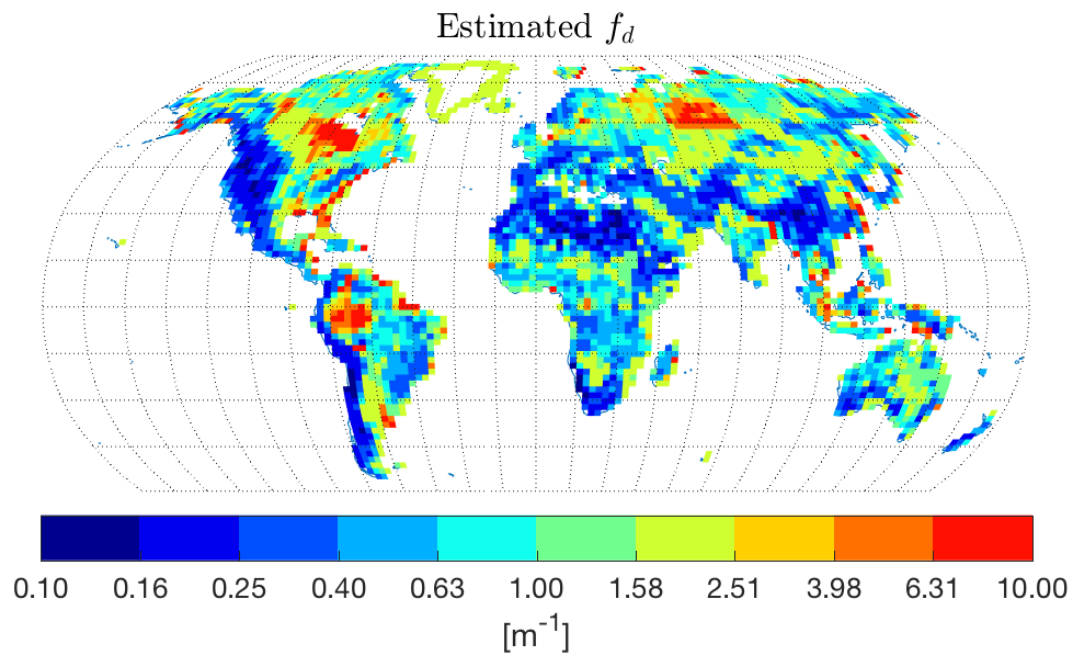
666

667 **Figure 5. Global estimate of f_d.**

668
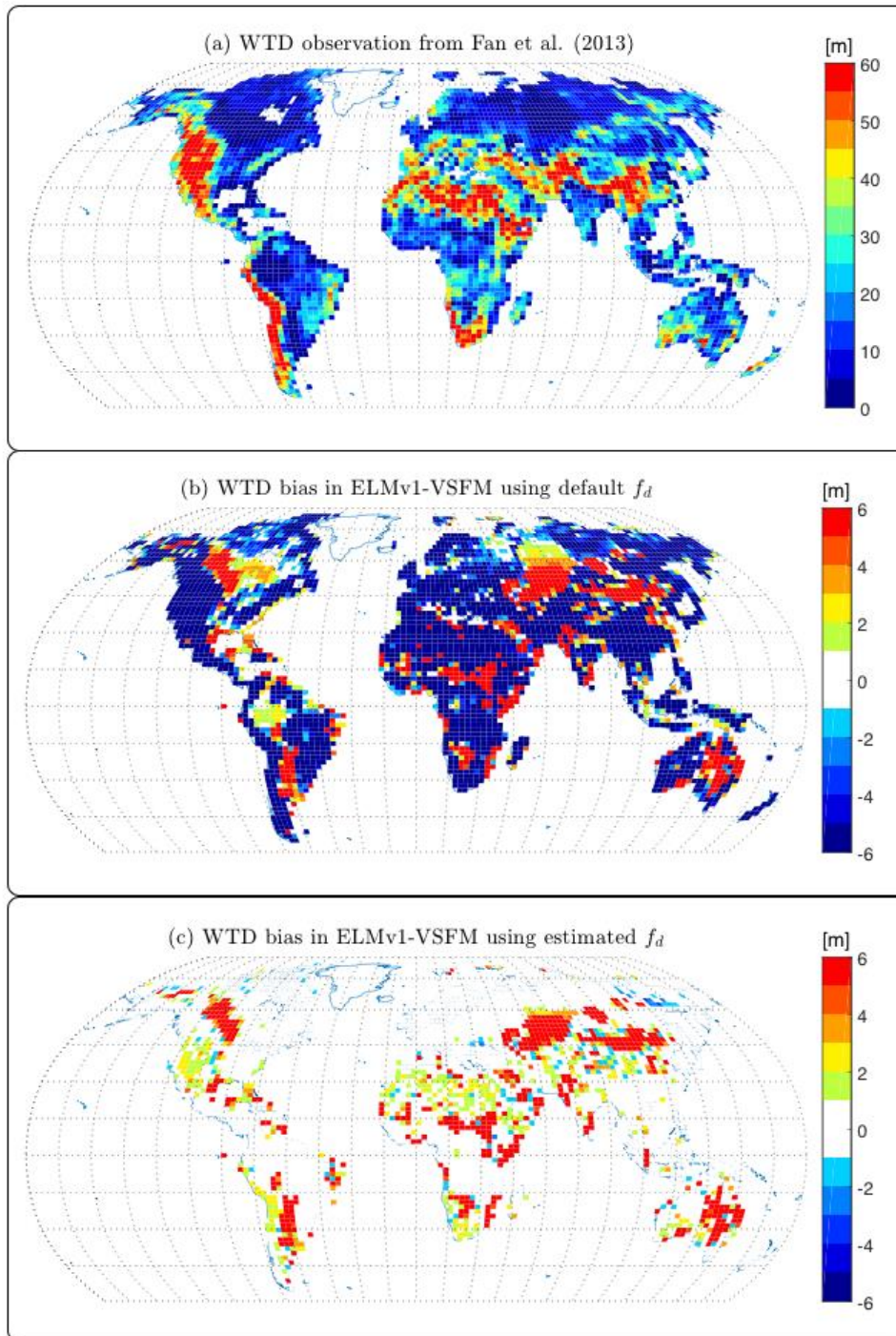
Figure 6. (a) Water table depth observation from Fan et al. (2013); (b) Water table depth biases (=Model – Obs) from ELMv1-VSFM using default spatially homogeneous f_d; and (c) Water table depth biases from ELMv1-VSFM using spatially heterogeneous f_d.

673
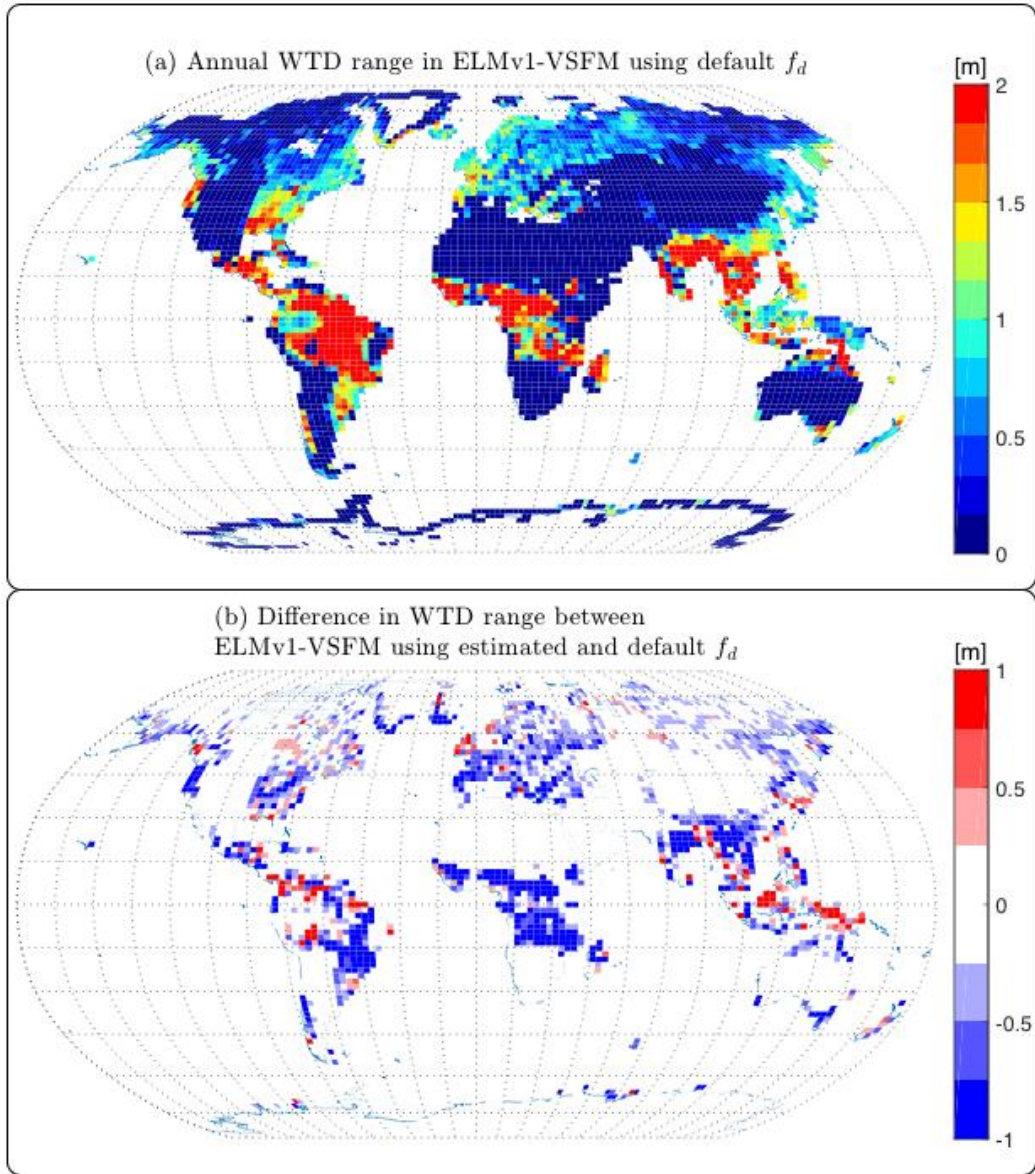
674

675 **Figure 7. (a) Annual range of water table depth for ELMv1-VSFM simulation**

676 **with spatially heterogeneous estimates of f_d and (b) Difference in annual**

677 **water table depth range between simulations with optimal and default f_d.**

678
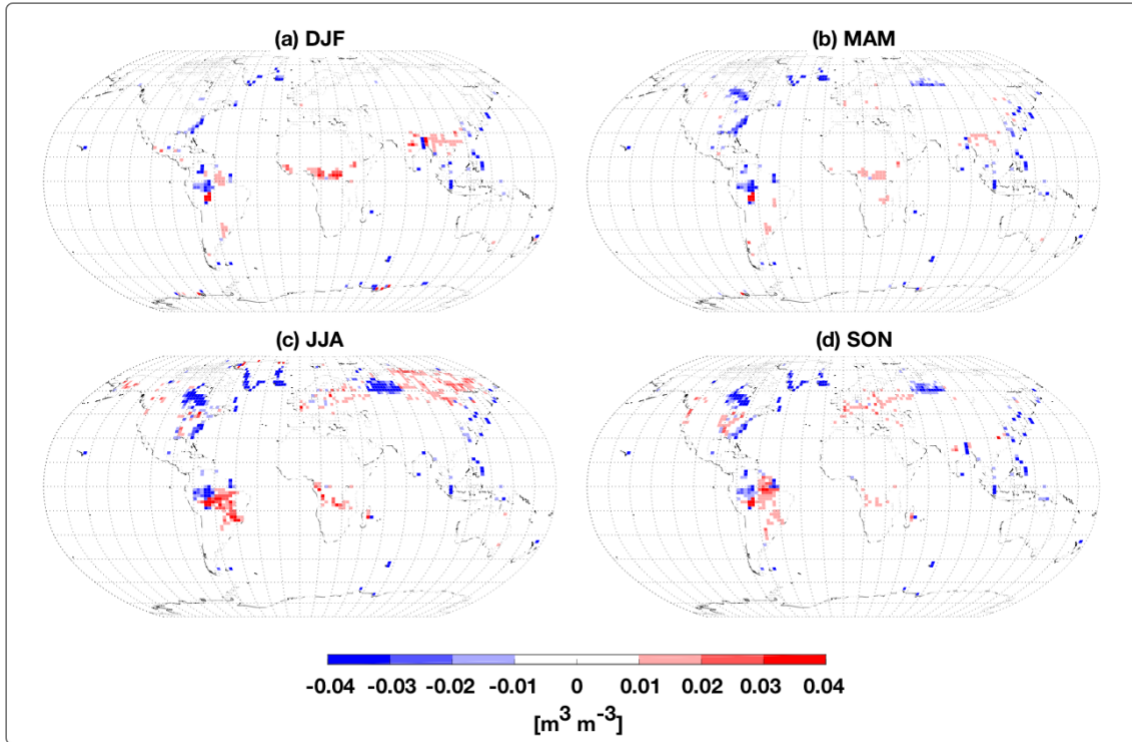
679

680 **Figure 8. Seasonal monthly mean soil moisture differences for top 10 cm**

681 **between ELMv1-VSFM simulations with optimal and default f_d values.**

682

684
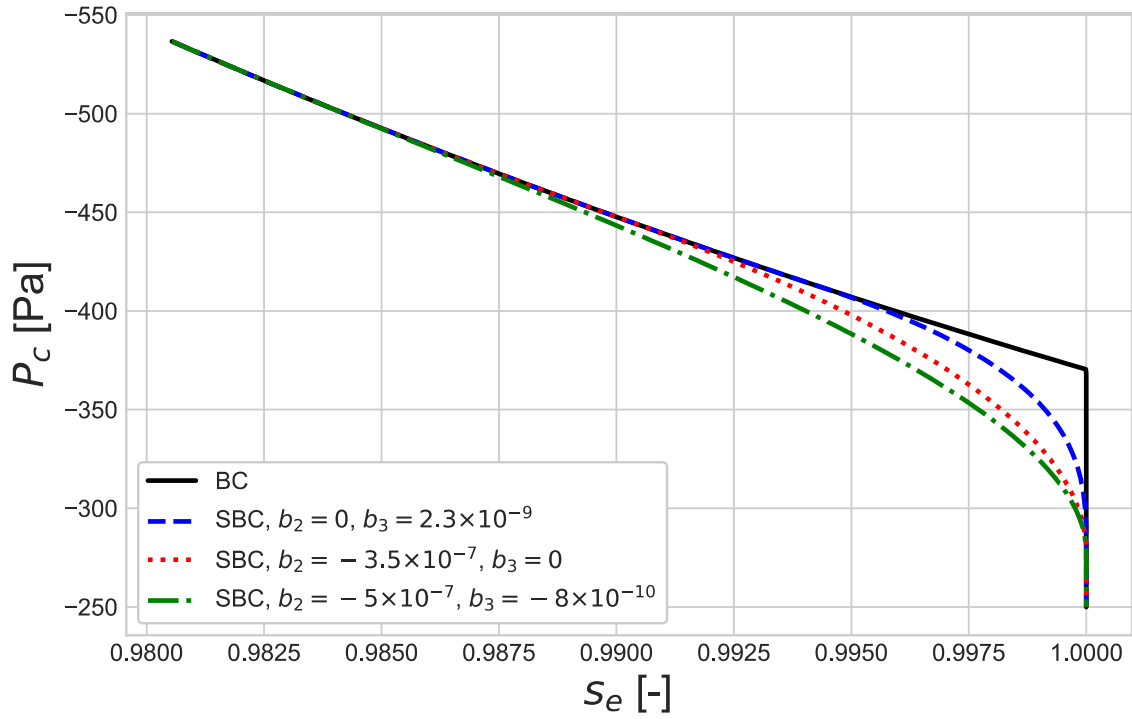
Figure A 1 The Brooks-Corey water rendition curve for estimating liquid saturation, S_e,

as a function of capillary pressure, P_c, shown in solid black line and smooth

approximation of Brooks-Corey (SBC) are shown in dashed line.

688

689 **References**

690 Alkhaier, F., Flerchinger, G. N., and Su, Z.: Shallow groundwater effect on land surface
691 temperature and surface energy balance under bare soil conditions: modeling and
692 description, Hydrol. Earth Syst. Sci., 16, 1817-1831, 2012.
693 Alley, W. M.: Ground Water and Climate, Ground Water, 39, 161-161, 2001.
694 Amenu, G. G. and Kumar, P.: A model for hydraulic redistribution incorporating
695 coupled soil-root moisture transport, Hydrol. Earth Syst. Sci., 12, 55-74, 2008.
696 Anyah, R. O., Weaver, C. P., Miguez-Macho, G., Fan, Y., and Robock, A.: Incorporating
697 water table dynamics in climate modeling: 3. Simulated groundwater influence on
698 coupled land-atmosphere variability, Journal of Geophysical Research: Atmospheres,
699 113, n/a-n/a, 2008.
700 Balay, S., Abhyankar , S., Adams, M. F., Brown, J., Brune, P., Buschelman, K., Dalcin, L.,
701 Eijkhout, V., Gropp, W. D., Kaushik, D., Knepley, M. G., McInnes, L. C., Rupp, K., Smith,
702 B. F., Zampini, S., Zhang, H., and Zhang, H.: PETSc Users Manual, Argonne National
703 LaboratoryANL-95/11 - Revision 3.7, 1-241 pp., 2016.
704 Banks, E. W., Brunner, P., and Simmons, C. T.: Vegetation controls on variably
705 saturated processes between surface water and groundwater and their impact on the
706 state of connection, Water Resources Research, 47, n/a-n/a, 2011.
707 Bense, V. F., Kooi, H., Ferguson, G., and Read, T.: Permafrost degradation as a control
708 on hydrogeological regime shifts in a warming climate, Journal of Geophysical
709 Research: Earth Surface, 117, 2012.
710 Bernhardt, M., Schulz, K., Liston, G. E., and Zängl, G.: The influence of lateral snow
711 redistribution processes on snow melt and sublimation in alpine regions, Journal of
712 Hydrology, 424–425, 196-206, 2012.
713 Beven, K. J. and Kirkby, M. J.: A physically based, variable contributing area model of
714 basin hydrology / Un modèle à base physique de zone d'appel variable de l'hydrologie
715 du bassin versant, Hydrological Sciences Bulletin, 24, 43-69, 1979.
716 Bisht, G., Huang, M., Zhou, T., Chen, X., Dai, H., Hammond, G. E., Riley, W. J., Downs, J. L.,
717 Liu, Y., and Zachara, J. M.: Coupling a three-dimensional subsurface flow and transport
718 model with a land surface model to simulate stream–aquifer–land interactions
719 (CP v1.0), Geosci. Model Dev., 10, 4539-4562, 2017.
720 Bisht, G., Riley, W. J., Wainwright, H. M., Dafflon, B., Yuan, F., and Romanovsky, V. E.:
721 Impacts of microtopographic snow redistribution and lateral subsurface processes
722 on hydrologic and thermal states in an Arctic polygonal ground ecosystem: a case
723 study using ELM-3D v1.0, Geosci. Model Dev., 11, 61-76, 2018.
724 Bohrer, G., Mourad, H., Laursen, T. A., Drewry, D., Avissar, R., Poggi, D., Oren, R., and
725 Katul, G. G.: Finite element tree crown hydrodynamics model (FETCH) using porous
726 media flow within branching elements: A new representation of tree hydrodynamics,
727 Water Resources Research, 41, n/a-n/a, 2005.
728 Brooks, R. H. and Corey, A. T.: Hydraulic properties of porous media, Colorado State
729 University, Fort Collins, CO, 1964.
730 Brown, J., Knepley, M. G., May, D. A., McInnes, L. C., and Smith, B.: Composable linear
731 solvers for multiphysics, 2012, 55-62.
732 Brunke, M. A., Broxton, P., Pelletier, J., Gochis, D., Hazenberg, P., Lawrence, D. M.,
733 Leung, L. R., Niu, G.-Y., Troch, P. A., and Zeng, X.: Implementing and Evaluating Variable

734 Soil Thickness in the Community Land Model, Version 4.5 (CLM4.5), Journal of
735 Climate, 29, 3441-3461, 2016.

736 Celia, M. A., Bouloutas, E. T., and Zarba, R. L.: A general mass-conservative numerical
737 solution for the unsaturated flow equation, Water Resources Research, 26, 1483-
738 1496, 1990.

739 Chen, J. and Kumar, P.: Topographic Influence on the Seasonal and Interannual
740 Variation of Water and Energy Balance of Basins in North America, Journal of Climate,
741 14, 1989-2014, 2001.

742 Chen, X. and Hu, Q.: Groundwater influences on soil moisture and surface evaporation,
743 Journal of Hydrology, 297, 285-300, 2004.

744 Chen, Y., Chen, Y., Xu, C., Ye, Z., Li, Z., Zhu, C., and Ma, X.: Effects of ecological water
745 conveyance on groundwater dynamics and riparian vegetation in the lower reaches
746 of Tarim River, China, Hydrological Processes, 24, 170-177, 2010.

747 Clapp, R. B. and Hornberger, G. M.: Empirical equations for some soil hydraulic
748 properties, Water Resources Research, 14, 601-604, 1978.

749 Clark, M. P., Fan, Y., Lawrence, D. M., Adam, J. C., Bolster, D., Gochis, D. J., Hooper, R. P.,
750 Kumar, M., Leung, L. R., Mackay, D. S., Maxwell, R. M., Shen, C., Swenson, S. C., and Zeng,
751 X.: Improving the representation of hydrologic processes in Earth System Models,
752 Water Resources Research, 51, 5929-5956, 2015.

753 Collier, N., Hoffman, F. M., Lawwrence, D. M., Keppel-Aleks, G., Koven, C. D., Riley, W.
754 J., Mu, M., and Randerson, J. T.: The International Land 1 Model Benchmarking
755 (ILAMB) System: Design, Theory, and Implementation, in review J. Advances in
756 Modeling Earth Systems, 2018. 2018.

757 Dai, A. and Trenberth, K. E.: Estimates of Freshwater Discharge from Continents:
758 Latitudinal and Seasonal Variations, Journal of Hydrometeorology, 3, 660-687, 2002.

759 Dams, J., Woldeamlak, S. T., and Batelaan, O.: Predicting land-use change and its
760 impact on the groundwater system of the Kleine Nete catchment, Belgium, Hydrol.
761 Earth Syst. Sci., 12, 1369-1385, 2008.

762 Dennis, J. M., Vertenstein, M., Worley, P. H., Mirin, A. A., Craig, A. P., Jacob, R., and
763 Mickelson, S.: Computational performance of ultra-high-resolution capability in the
764 Community Earth System Model, The International Journal of High Performance
765 Computing Applications, 26, 5-16, 2012.

766 E3SM Project, D.: Energy Exascale Earth System Model. 2018.

767 Fan, Y., Li, H., and Miguez-Macho, G.: Global Patterns of Groundwater Table Depth,
768 Science, 339, 940-943, 2013.

769 Fan, Y., Miguez-Macho, G., Weaver, C. P., Walko, R., and Robock, A.: Incorporating
770 water table dynamics in climate modeling: 1. Water table observations and
771 equilibrium water table simulations, Journal of Geophysical Research: Atmospheres,
772 112, n/a-n/a, 2007.

773 Farthing, M. W., Kees, C. E., and Miller, C. T.: Mixed finite element methods and higher
774 order temporal approximations for variably saturated groundwater flow, Advances
775 in Water Resources, 26, 373-394, 2003.

776 Ferguson, I. M. and Maxwell, R. M.: Human impacts on terrestrial hydrology: climate
777 change versus pumping and irrigation, Environmental Research Letters, 7, 044022,
778 2012.

779 Frampton, A., Painter, S., Lyon, S. W., and Destouni, G.: Non-isothermal, three-phase
780 simulations of near-surface flows in a model permafrost system under seasonal
781 variability and climate change, Journal of Hydrology, 403, 352-359, 2011.
782 Ghimire, B., Riley, W. J., Koven, C. D., Mu, M., and Randerson, J. T.: Representing leaf
783 and root physiological traits in CLM improves global carbon and nitrogen cycling
784 predictions, Journal of Advances in Modeling Earth Systems, 8, 598-613, 2016.
785 Grant, R. F., Humphreys, E. R., and Lafleur, P. M.: Ecosystem CO_2 and CH_4 exchange in
786 a mixed tundra and a fen within a hydrologically diverse Arctic landscape: 1. Modeling
787 versus measurements, Journal of Geophysical Research: Biogeosciences, 120, 1366-
788 1387, 2015.
789 Grant, R. F., Mekonnen, Z. A., Riley, W. J., Wainwright, H. M., Graham, D., and Torn, M.
790 S.: Mathematical Modelling of Arctic Polygonal Tundra with Ecosys: 1.
791 Microtopography Determines How Active Layer Depths Respond to Changes in
792 Temperature and Precipitation, Journal of Geophysical Research: Biogeosciences,
793 122, 3161-3173, 2017.
794 Green, T. R., Taniguchi, M., Kooi, H., Gurdak, J. J., Allen, D. M., Hiscock, K. M., Treidel, H.,
795 and Aureli, A.: Beneath the surface of global change: Impacts of climate change on
796 groundwater, Journal of Hydrology, 405, 532-560, 2011.
797 Gutmann, E. D. and Small, E. E.: The effect of soil hydraulic properties vs. soil texture
798 in land surface models, Geophysical Research Letters, 32, 2005.
799 Hammond, G. E. and Lichtner, P. C.: Field-scale model for the natural attenuation of
800 uranium at the Hanford 300 Area using high-performance computing, Water
801 Resources Research, 46, n/a-n/a, 2010.
802 Hilberts, A. G. J., Troch, P. A., and Paniconi, C.: Storage-dependent drainable porosity
803 for complex hillslopes, Water Resources Research, 41, n/a-n/a, 2005.
804 Hoffman, F. M., Koven, C. D., Keppel-Aleks, G., Lawrence, D. M., Riley, W. J., Randerson,
805 J. T., Ahlstrom, A., Abramowitz, G., Baldocchi, D. D., Best, M. J., Bond-Lamberty, B.,
806 Kauwe}, M. G. D., Denning, A. S., Desai, A. R., Eyring, V., Fisher, J. B., Fisher, R. A.,
807 Gleckler, P. J., Huang, M., Hugelius, G., Jain, A. K., Kiang, N. Y., Kim, H., Koster, R. D.,
808 Kumar, S. V., Li, H., Luo, Y., Mao, J., McDowell, N. G., Mishra, U., Moorcroft, P. R., Pau, G.
809 S. H., Ricciuto, D. M., Schaefer, K., Schwalm, C. R., Serbin, S. P., Shevliakova, E., Slater,
810 A. G., Tang, J., Williams, M., Xia, J., Xu, C., Joseph, R., and Koch, D.: International Land
811 Model Benchmarking (ILAMB) 2016 Workshop Report, U.S. Department of Energy,
812 Office of Science, 159 pp., 2017.
813 Hou, Z., Huang, M., Leung, L. R., Lin, G., and Ricciuto, D. M.: Sensitivity of surface flux
814 simulations to hydrologic parameters based on an uncertainty quantification
815 framework applied to the Community Land Model, Journal of Geophysical Research:
816 Atmospheres, 117, n/a-n/a, 2012.
817 Hwang, T., Band, L. E., Vose, J. M., and Tague, C.: Ecosystem processes at the watershed
818 scale: Hydrologic vegetation gradient as an indicator for lateral hydrologic
819 connectivity of headwater catchments, Water Resources Research, 48, n/a-n/a, 2012.
820 Ji, P., Yuan, X., and Liang, X.-Z.: Do Lateral Flows Matter for the Hyperresolution Land
821 Surface Modeling?, Journal of Geophysical Research: Atmospheres, doi:
822 10.1002/2017JD027366, 2017. n/a-n/a, 2017.

823 Jiang, X., Niu, G.-Y., and Yang, Z.-L.: Impacts of vegetation and groundwater dynamics
824 on warm season precipitation over the Central United States, Journal of Geophysical
825 Research: Atmospheres, 114, n/a-n/a, 2009.
826 Jung, M., Reichstein, M., and Bondeau, A.: Towards global empirical upscaling of
827 FLUXNET eddy covariance observations: validation of a model tree ensemble
828 approach using a biosphere model, Biogeosciences, 6, 2001-2013, 2009.
829 Kane, D. L., Hinkel, K. M., Goering, D. J., Hinzman, L. D., and Outcalt, S. I.: Non-
830 conductive heat transfer associated with frozen soils, Global and Planetary Change,
831 29, 275-292, 2001.
832 Kees, C. E. and Miller, C. T.: Higher order time integration methods for two-phase flow,
833 Advances in Water Resources, 25, 159-177, 2002.
834 Kim, H., Yeh, P. J. F., Oki, T., and Kanae, S.: Role of rivers in the seasonal variations of
835 terrestrial water storage over global basins, Geophysical Research Letters, 36, n/a-
836 n/a, 2009.
837 Kollet, S. J. and Maxwell, R. M.: Capturing the influence of groundwater dynamics on
838 land surface processes using an integrated, distributed watershed model, Water
839 Resources Research, 44, n/a-n/a, 2008.
840 Koster, R. D., Suarez, M. J., Ducharne, A., Stieglitz, M., and Kumar, P.: A catchment-
841 based approach to modeling land surface processes in a general circulation model: 1.
842 Model structure, Journal of Geophysical Research: Atmospheres, 105, 24809-24822,
843 2000.
844 Kundzewicz, Z. W. and Doli, P.: Will groundwater ease freshwater stress under climate
845 change?, Hydrological Sciences Journal, 54, 665-675, 2009.
846 Lasslop, G., Reichstein, M., Papale, D., Richardson, A. D., Arneth, A., Barr, A., Stoy, P.,
847 and Wohlfahrt, G.: Separation of net ecosystem exchange into assimilation and
848 respiration using a light response curve approach: critical issues and global
849 evaluation, Global Change Biology, 16, 187-208, 2010.
850 Leng, G., Huang, M., Tang, Q., and Leung, L. R.: A modeling study of irrigation effects
851 on global surface water and groundwater resources under a changing climate, Journal
852 of Advances in Modeling Earth Systems, 7, 1285-1304, 2015.
853 Leng, G., Leung, L. R., and Huang, M.: Significant impacts of irrigation water sources
854 and methods on modeling irrigation effects in the ACMELand Model, Journal of
855 Advances in Modeling Earth Systems, 9, 1665-1683, 2017.
856 Leung, L. R., Huang, M., Qian, Y., and Liang, X.: Climate–soil–vegetation control on
857 groundwater table dynamics and its feedbacks in a climate model, Climate Dynamics,
858 36, 57-81, 2011.
859 Levine, J. B. and Salvucci, G. D.: Equilibrium analysis of groundwater–vadose zone
860 interactions and the resulting spatial distribution of hydrologic fluxes across a
861 Canadian Prairie, Water Resources Research, 35, 1369-1383, 1999.
862 Liang, X., Xie, Z., and Huang, M.: A new parameterization for surface and groundwater
863 interactions and its impact on water budgets with the variable infiltration capacity
864 (VIC) land surface model, Journal of Geophysical Research: Atmospheres, 108, n/a-
865 n/a, 2003.
866 Lohse, K. A., Brooks, P. D., McIntosh, J. C., Meixner, T., and Huxman3, T. E.: Interactions
867 Between Biogeochemistry and Hydrologic Systems, Annual Review of Environment
868 and Resources, 34, 65-96, 2009.

869   Manoli, G., Bonetti, S., Domec, J.-C., Putti, M., Katul, G., and Marani, M.: Tree root
870   systems competing for soil moisture in a 3D soil–plant model, Advances in Water
871   Resources, 66, 32-42, 2014.
872   Marvel, K., Biasutti, M., Bonfils, C., Taylor, K. E., Kushnir, Y., and Cook, B. I.: Observed
873   and Projected Changes to the Precipitation Annual Cycle, Journal of Climate, 30, 4983-
874   4995, 2017.
875   Maxwell, R. M. and Miller, N. L.: Development of a Coupled Land Surface and
876   Groundwater Model, Journal of Hydrometeorology, 6, 233-247, 2005.
877   McDowell, N. G. and Allen, C. D.: Darcy's law predicts widespread forest mortality
878   under climate warming, Nature Clim. Change, 5, 669-672, 2015.
879   Miguez-Macho, G., Fan, Y., Weaver, C. P., Walko, R., and Robock, A.: Incorporating
880   water table dynamics in climate modeling: 2. Formulation, validation, and soil
881   moisture simulation, Journal of Geophysical Research: Atmospheres, 112, n/a-n/a,
882   2007.
883   Milly, P. C. D., Malyshev, S. L., Shevliakova, E., Dunne, K. A., Findell, K. L., Gleeson, T.,
884   Liang, Z., Phillipps, P., Stouffer, R. J., and Swenson, S.: An Enhanced Model of Land
885   Water and Energy for Global Hydrologic and Earth-System Studies, Journal of
886   Hydrometeorology, 15, 1739-1761, 2014.
887   Mualem, Y.: A new model for predicting the hydraulic conductivity of unsaturated
888   porous media, Water Resources Research, 12, 513-522, 1976.
889   Niu, G.-Y., Yang, Z.-L., Dickinson, R. E., and Gulden, L. E.: A simple TOPMODEL-based
890   runoff parameterization (SIMTOP) for use in global climate models, Journal of
891   Geophysical Research: Atmospheres, 110, n/a-n/a, 2005.
892   Niu, G.-Y., Yang, Z.-L., Dickinson, R. E., Gulden, L. E., and Su, H.: Development of a simple
893   groundwater model for use in climate models and evaluation with Gravity Recovery
894   and Climate Experiment data, Journal of Geophysical Research: Atmospheres, 112,
895   n/a-n/a, 2007.
896   Niu, J., Shen, C., Chambers, J. Q., Melack, J. M., and Riley, W. J.: Interannual Variation in
897   Hydrologic Budgets in an Amazonian Watershed with a Coupled Subsurface–Land
898   Surface Process Model, Journal of Hydrometeorology, 18, 2597-2617, 2017.
899   Oleson, K. W., D.M. Lawrence, G.B. Bonan, B. Drewniak, M. Huang, C.D. Koven, S. Levis,
900   F. Li, W.J. Riley, Z.M. Subin, S.C. Swenson, P.E. Thornton, A. Bozbiyik, R. Fisher, E.
901   Kluzek, J.-F. Lamarque, P.J. Lawrence, L.R. Leung, W. Lipscomb, S. Muszala, D.M.
902   Ricciuto, W. Sacks, Y. Sun, J. Tang, Z.-L. Yang: Technical Description of version 4.5 of
903   the Community Land Model (CLM), National Center for Atmospheric Research,
904   Boulder, CO, 422 pp., 2013.
905   Pacific, V. J., McGlynn, B. L., Riveros-Iregui, D. A., Welsch, D. L., and Epstein, H. E.:
906   Landscape structure, groundwater dynamics, and soil water content influence soil
907   respiration   across   riparian–hillslope   transitions   in   the   Tenderfoot   Creek
908   Experimental Forest, Montana, Hydrological Processes, 25, 811-827, 2011.
909   Pelletier, J. D., Broxton, P. D., Hazenberg, P., Zeng, X., Troch, P. A., Niu, G.-Y., Williams,
910   Z., Brunke, M. A., and Gochis, D.: A gridded global data set of soil, intact regolith, and
911   sedimentary deposit thicknesses for regional and global land surface modeling,
912   Journal of Advances in Modeling Earth Systems, 8, 41-65, 2016.

913   Petra, D.: Vulnerability to the impact of climate change on renewable groundwater
914   resources: a global-scale assessment, Environmental Research Letters, 4, 035006,
915   2009.
916   Piao, S. L., Ito, A., Li, S. G., Huang, Y., Ciais, P., Wang, X. H., Peng, S. S., Nan, H. J., Zhao, C.,
917   Ahlström, A., Andres, R. J., Chevallier, F., Fang, J. Y., Hartmann, J., Huntingford, C., Jeong,
918   S., Levis, S., Levy, P. E., Li, J. S., Lomas, M. R., Mao, J. F., Mayorga, E., Mohammat, A.,
919   Muraoka, H., Peng, C. H., Peylin, P., Poulter, B., Shen, Z. H., Shi, X., Sitch, S., Tao, S., Tian,
920   H. Q., Wu, X. P., Xu, M., Yu, G. R., Viovy, N., Zaehle, S., Zeng, N., and Zhu, B.: The carbon
921   budget of terrestrial ecosystems in East Asia over the last two decades,
922   Biogeosciences, 9, 3571-3586, 2012.
923   Pruess, K., Oldenburg, C., and Moridis, G.: TOUGH2 User's Guide, Version 2.0,
924   Lawrence Berkeley National Laboratory, Berkeley, CALBNL-43134, 1999.
925   Rihani, J. F., Maxwell, R. M., and Chow, F. K.: Coupling groundwater and land surface
926   processes: Idealized simulations to identify effects of terrain and subsurface
927   heterogeneity on land surface energy fluxes, Water Resources Research, 46, n/a-n/a,
928   2010.
929   Salvucci, G. D. and Entekhabi, D.: Hillslope and Climatic Controls on Hydrologic Fluxes,
930   Water Resources Research, 31, 1725-1739, 1995.
931   Shen, C., Niu, J., and Phanikumar, M. S.: Evaluating controls on coupled hydrologic and
932   vegetation dynamics in a humid continental climate watershed using a subsurface-
933   land surface processes model, Water Resources Research, 49, 2552-2572, 2013.
934   Siebert, S., Burke, J., Faures, J. M., Frenken, K., Hoogeveen, J., Döll, P., and Portmann, F.
935   T.: Groundwater use for irrigation – a global inventory, Hydrol. Earth Syst. Sci., 14,
936   1863-1880, 2010.
937   Sivapalan, M., Beven, K., and Wood, E. F.: On hydrologic similarity: 2. A scaled model
938   of storm runoff production, Water Resources Research, 23, 2266-2278, 1987.
939   Soylu, M. E., Istanbulluoglu, E., Lenters, J. D., and Wang, T.: Quantifying the impact of
940   groundwater depth on evapotranspiration in a semi-arid grassland region, Hydrol.
941   Earth Syst. Sci., 15, 787-806, 2011.
942   Sperry, J. S., Adler, F. R., Campbell, G. S., and Comstock, J. P.: Limitation of plant water
943   use by rhizosphere and xylem conductance: results from a model, Plant, Cell &
944   Environment, 21, 347-359, 1998.
945   Srivastava, R. and Yeh, T. C. J.: Analytical solutions for one-dimensional, transient
946   infiltration toward the water table in homogeneous and layered soils, Water
947   Resources Research, 27, 753-762, 1991.
948   Swenson, S. C. and Lawrence, D. M.: Assessing a dry surface layer-based soil resistance
949   parameterization for the Community Land Model using GRACE and FLUXNET-MTE
950   data, Journal of Geophysical Research: Atmospheres, 119, 10,299-210,312, 2014.
951   Swenson, S. C., Lawrence, D. M., and Lee, H.: Improved simulation of the terrestrial
952   hydrological cycle in permafrost regions by the Community Land Model, Journal of
953   Advances in Modeling Earth Systems, 4, n/a-n/a, 2012.
954   Tanaka, M., Girard, G., Davis, R., Peuto, A., and Bignell, N.: Recommended table for the
955   density of water between 0 °C and 40 °C based on recent experimental reports,
956   Metrologia, 38, 301, 2001.
957   Taylor, K. E., Stouffer, R. J., and Meehl, G. A.: An Overview of CMIP5 and the Experiment
958   Design, Bulletin of the American Meteorological Society, 93, 485-498, 2012.

959 Taylor, R. G., Scanlon, B., Döll, P., Rodell, M., Van Beek, R., Wada, Y., Longuevergne, L.,
960 Leblanc, M., Famiglietti, J. S., and Edmunds, M.: Ground water and climate change,
961 Nature Climate Change, 3, 322-329, 2013.
962 Tian, W., Li, X., Cheng, G. D., Wang, X. S., and Hu, B. X.: Coupling a groundwater model
963 with a land surface model to improve water and energy cycle simulation, Hydrol.
964 Earth Syst. Sci., 16, 4707-4723, 2012.
965 van Genuchten, M. T.: A Closed-form Equation for Predicting the Hydraulic
966 Conductivity of Unsaturated Soils1, Soil Science Society of America Journal, 44, 892-
967 898, 1980.
968 Walko, R. L., Band, L. E., Baron, J., Kittel, T. G. F., Lammers, R., Lee, T. J., Ojima, D., Sr., R.
969 A. P., Taylor, C., Tague, C., Tremback, C. J., and Vidale, P. L.: Coupled Atmosphere–
970 Biophysics–Hydrology Models for Environmental Modeling, Journal of Applied
971 Meteorology, 39, 931-944, 2000.
972 White, M. and STOMP, O. M.: Subsurface transport over multiple phases; Version 2.0;
973 Theory Guide, Pacific Northwest National Laboratory, 2000. 2000.
974 Yeh, P. J.-F. and Eltahir, E. A. B.: Representation of Water Table Dynamics in a Land
975 Surface Scheme. Part I: Model Development, Journal of Climate, 18, 1861-1880, 2005.
976 York, J. P., Person, M., Gutowski, W. J., and Winter, T. C.: Putting aquifers into
977 atmospheric simulation models: an example from the Mill Creek Watershed,
978 northeastern Kansas, Advances in Water Resources, 25, 221-238, 2002.
979 Yuan, X., Xie, Z., Zheng, J., Tian, X., and Yang, Z.: Effects of water table dynamics on
980 regional climate: A case study over east Asian monsoon area, Journal of Geophysical
981 Research: Atmospheres, 113, n/a-n/a, 2008.
982 Zektser, I. S. and Evertt, L. G.: Groundwater resources of the world and their use,
983 United Nations Educational, Scientific and Cultural Organization7, place de Fontenoy,
984 75352 Paris 07 SP, 2004.
985 Zeng, X. and Decker, M.: Improving the Numerical Solution of Soil Moisture–Based
986 Richards Equation for Land Models with a Deep or Shallow Water Table, Journal of
987 Hydrometeorology, 10, 308-319, 2009.
988 Zhu, Q., Riley, W. J., Tang, J., and Koven, C. D.: Multiple soil nutrient competition
989 between plants, microbes, and mineral surfaces: model development,
990 parameterization, and example applications in several tropical forests,
991 Biogeosciences, 13, 341-363, 2016.
992
993